C.E. SACLAY
DSM

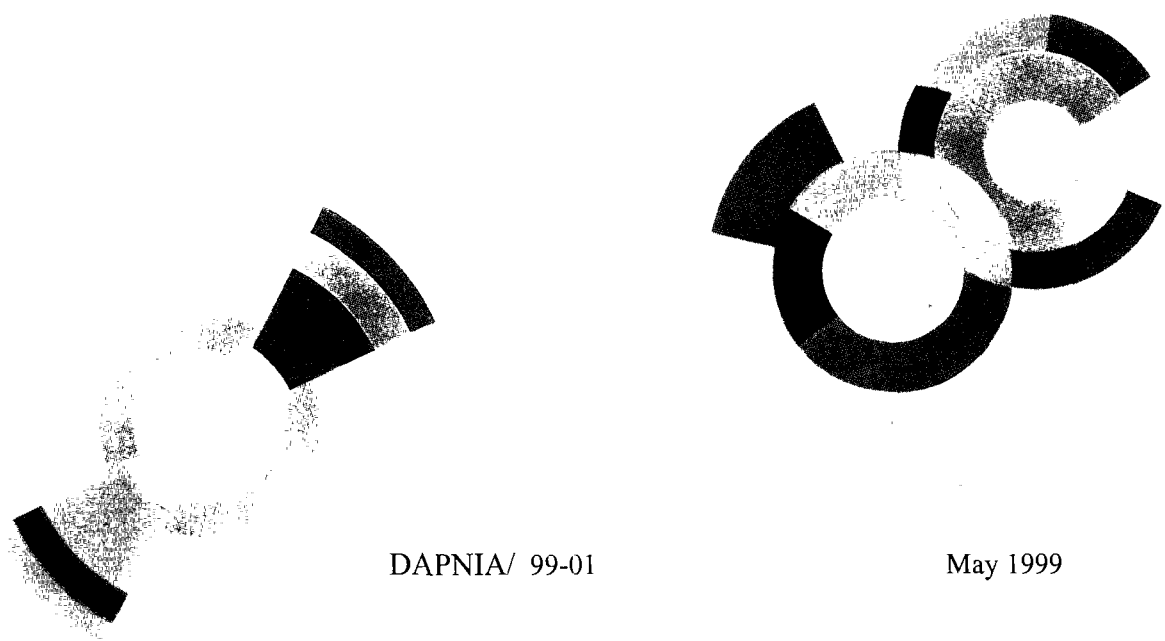

DAPNIA/ 99-01 May 1999

A DEEP SEA TELESCOPE FOR HIGH ENERGY NEUTRINOS

The ANTARES Collaboration

DAPNIA

DISCLAIMER

Portions of this document may be illegible in electronic image products. Images are produced from the best available original document.

A Deep Sea Telescope for High Energy Neutrinos

The ANTARES Collaboration

31 May, 1999

The ANTARES Collaboration

Particle Physics Institutes

E. Aslanides, J-J. Aubert, S. Basa, F. Bernard, V. Bertin, M. Billault, P-E. Blanc, J. Brunner, A. Calzas, F. Cassol, J. Carr, C. Carloganu, J-J. Destelle, P-Y. Duval, F. Hubaut, E. Kajfasz, M. Jaquet, D. Laugier, A. Le Van Suu, P.L. Liotard, L. Martin, F. Montanet, S. Navas, C. Olivetto, P. Payre, A. Pohl, R. Potheau, M. Raymond, M. Talby, C. Tao, E. Vigeolas.

Centre de Physique des Particules de Marseille (CPPM), (CNRS/IN2P3 - Université de la Méditerranée Aix-Marseille II), 163 Avenue de Luminy, Case 907, 13288 Marseille Cedex 09, France

S. Anvar, R. Azoulay, R. W. Bland, F. Blondeau, N. de Botton, N. Bottu, P-H. Carton, P. Deck, F. E. Desages, G. Dispau, F. Feinstein, P. Goret, L. Gosset, J-F. Gournay, J. R. Hubbard, M. Karolak, A. Kouchner, D. Lachartre, H. Lafoux, P. Lamare, J-C. Languillat, J-P. Laugier, H. Le Provost, S. Loucatos, P. Magnier, B. Mazeau, P. Mols, L. Moscoso, N. Palanque-Delabrouille, P. Perrin, J. Poinsignon, Y. Queinec, Y. Sacquin, J-P. Schuller, T. Stolarczyk, A. Tabary, Y. Tayalati, P. Vernin, D. Vignaud, D. Vilanova.

DAPNIA/DSM, CEA/Saclay, 91191 Gif sur Yvette Cedex, France

Y. Benhammou, F. Drouhin, D. Huss, A. Pallares, T. Tzvetanov.

Groupe de Recherches en Physique des Hautes Energies (GRPHE), (Université de Haute Alsace), 61 Rue Albert Camus, 68093 Mulhouse Cedex, France

M. Danilov, R. Kagan, A. Rostovstev.

Institute for Theoretical and Experimental Physics (ITEP), B. Cheremushkinskaya 25, 117259 Moscow, Russia

E. Carmona, R. Cases, J. J. Hernández, J. Zúñiga.

Instituto de Física Corpuscular, CSIC - Universitat de València, 46100 Burjassot, Valencia, Spain

C. Racca, A. Zghiche.

Institut de Recherches Subatomiques (IReS), (CNRS/IN2P3 - Université Louis Pasteur), BP 28, 67037 Strasbourg Cedex 2, France

R. van Dantzig, J. Engelen, A. Heijboer, M. de Jong, E. Kok, P. Kooijman, G.J. Nooren, J. Oberski, P. de Witt Huberts, E. de Wolf.
NIKHEF and University of Amsterdam, Kruislaan 409, PO Box 41882, 1009 BD Amsterdam, Netherlands

D. Evans, G. Mahout, I. Kenyon, P. Jovanovic, P. Newman, T. McMahon.
University of Birmingham, School of Physics and Astronomy, Edgbaston, Birmingham B15 2TT, United Kingdom

B. Brooks, S. Cooper, J. Fopma, N. Jelley, W. Schuster, S. Tilav, D. Wark.
University of Oxford, Department of Physics, Nuclear and Astrophysics Laboratory, Keble Road, Oxford OX1 3RH, United Kingdom

S. Cartwright, V. Kudryavtsev, J. McMillan, N. Spooner, L. Thompson.
University of Sheffield, Department of Physics and Astronomy, Sheffield, S3 7RH, United Kingdom

R. Triay.
Centre de Physique Théorique (CPT), (CNRS), 163 Avenue de Luminy, Case 907, 13288 Marseille Cedex 09, France

Astronomy Institutes

A. Mazure.
Laboratoire d'Astronomie Spatiale, Institut Gassendi pour la Recherche Astronomique en Provence (IGRAP), (CNRS/INSU - Université de Provence Aix-Marseille I), Les Trois Lucs, Traverse du Siphon, 13012 Marseille Cedex, France

P. Amram, J. Boulesteix, M. Marcelin.
Observatoire de Marseille, Institut Gassendi pour la Recherche Astronomique en Provence (IGRAP), (CNRS/INSU - Université de Provence Aix-Marseille I), 2 Place Le Verrier, 13248 Marseille Cedex 4, France

Sea Science Institutes

F. Blanc, G. Coustillier, J-L. Fuda, C. Millot.

Centre d'Océanologie de Marseille, (CNRS/INSU - Université de la Méditerranée), Station Marine d'Endoume-Luminy, Rue de la Batterie des Lions, 13007 Marseille, France

C. Compère, J.F. Drogou, D. Festy, G. Herrouin, Y. Le Guen, L. Lemoine, A. Massol, F. Mazéas, J.P. Morel, J.F. Rolin, P. Valdy.

IFREMER, Centre de Toulon/La Seyne sur Mer, Port Brégaillon, Chemin Jean-Marie Fritz, 83500 La Seyne sur Mer, France
IFREMER, Centre de Brest, 29280 Plouzané, France

Contents

Chapter 1

Introduction

This document presents the scientific motivation for building a high energy neutrino undersea detector, with an effective area of 0.1 km^2, along with a review of the technical issues involved in its design and construction. The planned apparatus consists of an array of photomultipliers, arranged in a lattice near the sea bed at a depth of 2400 m, to detect the Cherenkov light from muons produced by neutrino interactions in the seawater and rock beneath. Since 1996, the ANTARES collaboration has conducted an extensive R&D programme in close collaboration with experts in marine technology. This programme has addressed most of the critical technical aspects relevant to the construction and operation of a neutrino telescope, providing the information and experience necessary to be confident that the planned array is feasible at a reasonable cost. The neutrino detection capabilities of the design have been evaluated in detailed simulation studies and its potential science mission explored.

1.1 Why neutrino astronomy?

Most of our current knowledge of the Universe comes from the observation of photons. Photons have many advantages as cosmic information carriers: they are copiously produced, they are stable and electrically neutral, they are easy to detect over a wide energy range, and their spectrum carries detailed information about the chemical and physical properties of the source. Their disadvantage is that the hot, dense regions which form the central engines of stars, active galactic nuclei and other astrophysical energy sources

are completely opaque to photons, and therefore we cannot investigate the properties of these regions by direct observation, but only by indirect inference. For example, the photons we observe from the Sun come from its photosphere, far removed from the hydrogen-fusing core. Moreover, high energy photons interact with photons of the infrared radiation background and with the cosmic microwave background to create electron-positron pairs; this is the Greisen-Zatsepin-Kuz'min effect (GZK) [1]. This effect suppresses any possibility of surveying the sky over distances greater than 100 Mpc with high energy (>10 TeV) gamma rays.

In order to observe the inner workings of the astrophysical objects and to obtain a description of the Universe over a larger range of energies, we need a probe which is electrically neutral, so that its trajectory will not be affected by magnetic fields, stable so that it will reach us from distant sources, and weakly interacting so that it will penetrate regions which are opaque to photons. The only candidate currently known to exist is the neutrino.

Some astrophysical sources are known to emit neutrinos: hydrogen fusion produces electron neutrinos as by-products, and solar neutrino astronomy has a 30 years long history; the conversion of iron nuclei to neutrons when a neutron star is formed in the heart of a supernova produces a burst of neutrinos (augmented by the thermal production of neutrino-antineutrino pairs), and one such burst was observed by Kamiokande and IMB for Supernova 1987A; cosmology predicts a low-energy relic neutrino background similar to the low-energy relic photons of the Cosmic Microwave Background, but these would have an effective temperature of around 1.9 K and are very difficult to observe.

Astrophysical sources of high-energy neutrinos have not been observed directly, but their existence can be inferred from the properties of cosmic rays. Primary cosmic rays are protons, with some admixture of heavier nuclei; the energy spectrum is a power law which extends to extremely high energies, values exceeding 10^{20} eV having been observed in recent years. Protons themselves have limited use as astrophysical information carriers because they are charged, and therefore subject to deflection by cosmic magnetic fields: only the very highest-energy cosmic rays are likely to retain any memory of the source direction. The exact source of the high-energy cosmic rays is thus unknown, although supernova remnants and active galactic nuclei have been proposed. Whatever the source, it is clear that accelerating protons to such high energies is likely to generate a large associated flux of photo-produced pions, which decay to yield gamma rays and neutrinos. These will

remember the source direction, and so the existence of a general flux of very high energy cosmic-ray protons implies the existence of sources of high-energy neutrinos.

Neutrino astronomy thus offers the possibility of observing sources which correspond to the central engines of the most energetic astrophysical phenomena. As discussed below, it also provides long baselines for neutrino oscillation studies, and can explore useful regions of supersymmetric parameter space in the context of dark matter. The drawback, of course, is that the weak interactions of neutrinos imply that a very massive detector with extremely good background rejection is required to observe a measurable flux.

1.2 The view from a neutrino telescope

The ANTARES scientific programme is described in detail in chapter 2, but a brief overview is presented here. It is convenient to divide the programme into three broad subject areas: particle physics (neutrino oscillations), particle astrophysics (searches for neutralino dark matter) and astronomy.

Within the minimal standard model, neutrinos are strictly massless, but the need to incorporate non-zero masses has long been anticipated. Neutrino astronomy was instrumental in establishing non-zero neutrino masses as an important topic: the lower-than-predicted flux of electron neutrinos from the Sun (the Solar Neutrino Problem) is now generally believed to be explained by neutrino oscillations either *in vacuo* or more probably within the Sun itself, enhanced by the high electron density in the solar core (the MSW effect).

Neutrino oscillation solutions to the solar neutrino problem involve the conversion of electron neutrinos into some other flavour. The energies involved are not well matched to the detection capabilities of ANTARES. However, recent results from Super-Kamiokande appear to show a similar flux reduction occurring for *muon* neutrinos generated by cosmic-ray interactions at the top of the Earth's atmosphere. The effect is interpreted as evidence for the oscillation of ν_μ into either ν_τ or a so-called "sterile" neutrino, with a large mixing angle and a squared mass difference of $\sim 10^{-3} - 10^{-2}$ eV^2. This is a result of major importance which urgently requires confirmation by an experiment with independent systematics. As discussed below, the proposed ANTARES configuration should be capable of exploring the region

of parameter space favoured by the Super-Kamiokande data.

In recent years it has become generally accepted by astrophysicists that most of the matter in the universe is non-luminous "dark matter". The clearest evidence for this is the observed flatness of the rotation curves of disk galaxies, which imply a dynamical mass far in excess of that accounted for by the constituent stars and gas. Constraints from the observed abundances of light elements indicate that much of the dark matter in the cosmos must be non-baryonic. No presently known particle has the required properties, but a good theoretical candidate is the stable neutral particle expected in most versions of supersymmetry theory.

The detection and identification of a relic cosmological population of supersymmetric particles would be of immense importance to both cosmology and particle theory. Neutrino telescopes are not directly sensitive to a weakly interacting massive particle (WIMP). However, supersymmetric WIMPs will accumulate in the cores of the Sun and the Earth or in the centre of the Galaxy through gravitational capture. The resulting high space density leads to annihilation reactions, which will yield high-energy neutrinos through the decays of the gauge bosons and heavy particles produced. The proposed detector would be sensitive to these neutrinos over a useful range of WIMP masses. Compared to ongoing direct detection experiments, neutrino telescopes are generally more suitable for higher masses, although resonances in the Earth's capture cross-section enhance the signal strongly at certain lower masses, particularly around 56 GeV. But even a confirmation of a prior direct detection would provide useful information about the couplings of the WIMP, and thus help to constrain the parameters of the theory.

As discussed above, the two confirmed astrophysical neutrino sources are: the Sun and supernovae as exemplified by SN 1987A. Both of these produce low energy neutrinos which could not be tracked by ANTARES, although a nearby supernova could be detected through a transient increase in the overall singles rate. However, there are a number of candidate astrophysical sources of high-energy neutrinos which would be detected by ANTARES. Since pions produced by high-energy protons are the likeliest source of high-energy neutrinos, candidate astrophysical neutrino sources are the proton accelerators, which might explain the High Energy Cosmic Rays spectrum. High energy γ-rays may be associated with high energy protons and their subsequent decays from π^0, but they are also produced by synchrotron radiation of fast electrons in the presence of magnetic fields. The observation of neutrino sources would unambiguously discriminate between

the two acceleration mechanisms.

Candidate sources can be identified both within the Galaxy—accreting binaries containing neutron stars or black holes, supernovae and young supernova remnants—and elsewhere, most notably active galactic nuclei (AGN) and gamma-ray bursters. This represents a rich spectrum of possible sources, both steady and transient, covering a wide range of neutrino energies.

It is worth noting that the history of astronomical observation suggests that the likeliest outcome of opening a new observational window is the discovery of a completely unexpected class of sources. Such discoveries are by definition difficult to anticipate, but one possible pointer is that the very highest-energy cosmic rays, those above 10^{20} eV, remain difficult to explain in present models. This puzzle could be solved by the observation of their associated neutrinos.

1.3 Present and future neutrino telescopes

The proposed ANTARES detector is one of a number of present and proposed neutrino telescope projects. Of these, the Lake Baikal detector, consisting of eight strings supporting a total of 192 optical modules, was the first to demonstrate the feasibility of the technique, but is limited in depth and spatial extent by the nature of its site and so cannot be extended to a full-scale neutrino telescope. The AMANDA array at the South Pole uses ice rather than water as the detector medium, which gives it lower backgrounds but poorer directional accuracy. An array with an effective area of around 10^4 m^2, AMANDA B, has been deployed at a depth of 1500–2000 m and has published data on atmospheric muons; the installation of AMANDA-II, which will have an effective area several times larger, has started during the 1997–98 season. An eventual scale-up to a full km-scale array (ICECUBE) is proposed. Also at the proposal stage is NESTOR, with a deep site in the eastern Mediterranean off Pylos (Greece).

The present ANTARES proposal is in many respects complementary to AMANDA. A water-based detector is more flexible and has better directional sensitivity, at the cost of higher background noise. Together, the two detectors cover the whole sky, with a substantial amount of overlap for cross-checking.

The Mediterranean Sea represents an environment for a neutrino telescope that is quite different from those of the operating arrays at Lake

Baikal (a freshwater lake which freezes over in winter) and the South Pole. Therefore, since its creation in 1996, ANTARES has followed a first phase R&D programme focused on three major milestones:

- construction and deployment of test lines dedicated to measuring environmental parameters such as optical background, biofouling and water transparency;
- development of prototype strings to acquire the necessary expertise to deploy and operate an undersea detector up to the kilometre scale;
- development of software tools to explore the physics capabilities of the detector.

To date, the majority of the deployments have been performed in the Mediterranean Sea 30 km off the coast near Toulon (France), at a depth of 2400 m.

This first phase has demonstrated that the deployment and physics operation of such a detector is feasible. The present proposal advances the ANTARES programme to a second phase, namely the construction of an array of 1000 optical modules to form a high-energy neutrino detector with effective area 0.1 km^2. Such an array would have the following achievable physics goals:

- the study of the high energy neutrino flux (in the TeV–PeV range) with unprecedented angular resolution;
- the measurement of atmospheric neutrino oscillations in the region of parameter space favoured by Super-Kamiokande;
- a search for supersymmetric dark matter covering a region of model parameter space which is interesting for cosmology and particle physics.

It would also provide practical experience and expertise which will be invaluable for the anticipated third phase during which a larger scale detector will be constructed, capable of conducting a search for astrophysical sources.

Chapter 2

Scientific programme

The science mission of a neutrino telescope such as ANTARES is vast, encompassing neutrino astronomy, neutrino oscillations and non-baryonic matter in the form of neutralinos, heavy metastable relic particles or topological defects. This chapter gives a brief account of the physics of the main candidate neutrino sources and the mechanisms by which they might produce a significant signal.

2.1 Astrophysical sources

The principal mechanism for generating high energy neutrinos is through decay cascades induced by high energy protons. Interactions of protons with matter or radiation produce mesons whose leptonic decay modes will yield neutrinos. A list of possible high energy astrophysical neutrino sources therefore involves a list of candidate astrophysical sites for proton acceleration.

2.1.1 X-ray binaries

This class of binary stars, which are among the brightest cosmic X-ray sources, consists of compact objects, such as neutron stars or black holes, which accrete matter from their normal companion stars. The accretion process leads to plasma waves in the strong magnetic field of the compact object, which bring protons to high energies by stochastic acceleration. Interactions of the accelerated particles with the accreting matter or with

the companion star would then produce a neutrino flux comparable to that in high-energy particles with a spectral index close to 2.

2.1.2 Supernova remnants and cosmic rays

Explosions of massive stars (supernovae) produce an expanding shell of material which is known from radio observations to accelerate high-energy particles. In some cases, the residue of the supernova is a neutron star which is detectable as a pulsar. Protons inside supernova shells can be accelerated by a first-order Fermi mechanism if (as seems likely) the shell is turbulent. If a pulsar is present there are additional acceleration mechanisms: in the magnetosphere of the pulsar, or at the front of the shock wave produced by the magneto-hydrodynamic wind in the shell [2]. The interaction of these protons with the matter of the shell gives rise to neutrinos and photons (from charged and neutral pion decays respectively). An especially promising source is the ion doped wind model based on ultra high energy ion acceleration by the pulsar [3]. The ions drift across the magnetic field in the surrounding supernova remnant filaments at a speed of order 10 times the hydrodynamic expansion velocity and interact with the thermal gas to produce neutrinos via $\pi^{\pm}$ production. The minimum flux predicted is substantially above background for the Crab remnant at 10^{16} eV, but the theory of ion acceleration is too primitive to constrain the spectrum of injected ions and hence the production rate of energetic neutrinos at ANTARES energies.

It is thought that supernova remnants are the principal galactic source of cosmic-ray protons, but, as yet, there is no direct confirmation of this hypothesis. Recent observations [4] above 10^8 eV by the EGRET detector have found $\gamma-$ray signals associated with at least 2 supernova remnants (IC 443 and γ Cygni). However, electromagnetic radiation is an ambiguous signature, as it can come from either accelerated electrons or protons. An observation of neutrinos would provide a clear indication of proton acceleration with the direction identifying the source.

2.1.3 Active galactic nuclei

Active Galactic Nuclei (AGN) such as quasars are, averaged over time, the most powerful known objects in the Universe. Their observed total luminosities are in the range $10^{35} - 10^{41}$ W [5]. In the generic model of

AGN, these high luminosities arise from accretion of matter, at a rate of at least a few solar masses per year, onto a super-massive black hole, ranging from 10^6 to 10^{10} solar masses. A minority of AGN also produces relativistic jets which transport synchrotron-emitting electrons, most easily observable in the radio, over distances up to 1 Mpc. Objects of this type whose jets are directed almost exactly towards us appear as intense, compact and variable sources because their emission is amplified by Doppler boosting. Such objects are known as "blazars".

An unexpected result, now well established by the EGRET satellite [6], is that many blazars emit γ rays with energies up to $\approx 10^{10}$ eV. Even more surprisingly, four members of this class have been detected by atmospheric

2.1.4 Gamma ray bursts

Gamma Ray Bursts (GRBs) are the most spectacularly violent phenomena in the universe known to this date, and up until two years ago they were declared to be one of the outstanding mysteries of modern astrophysics. However, early 1997 brought a major break though when the BeppoSAX satellite [11] located a burst precisely enough to permit the identification of its optical counterpart. Since then, further advances have been made, with the discovery of GRB afterglows, measurements of their redshift and recognition of the magnitude of the energy release occurring in these second-long flashes.

So far about a dozen GRB afterglows have been detected. The distances measured place the burst sources at cosmological distances with redshifts in the range $z = 0.8 - 3.4$ and indicate an energy release of $10^{45\pm1}$ J in γ-rays alone (assuming isotropic emission). The location of GRBs in their host galaxies somewhat correlates the population of GRB progenitors with the star formation rates, and supports models which involve a black hole formation through coalescence of a binary system of either a black hole-neutron star or a neutron star-neutron star.

Detailed studies of afterglows from X-rays to optical and radio wavelengths provided crucial constraints on physical parameters for theoretical models. In the current standard model for γ-ray bursts and their afterglows, the *fireball-plus-blastwave* model [12], the initial event deposits a solar mass of energy into a region with a radius of about 100 km. The resulting fireball expands ultra-relativistically with Lorentz factor $\gamma \geq 300$ into the surrounding medium. While the forward shock sweeps material and heats it, the reverse shock collides with the ejecta. Therefore, the afterglow is produced by synchrotron radiation when external shocks decelerate. However, the multi-peaked light curve of the gamma-ray burst itself is produced by the collisions of several internal shocks which are catching up each other with different Lorentz factors within the inner engine. There is clear evidence of these three distinct regions of the fireball in the light curve of GRB990123 [13].

A hadronic component would naturally be expected in such extreme phenomena. Nearby GRBs could therefore be the long sought after sources of the highest energy cosmic rays. A possible example of such a relatively local GRB is GRB980425, whose location was observed to be coincident with the extremely bright supernova SN 1998bw. If this association is real, the

GRB occurred at a distance of a few Mpc[14] and is a potential source of ultra-high-energy cosmic rays. In such a case, the cosmic ray observations set a model independent upper bound to the flux of high energy neutrinos produced by photo-meson interactions of the high energy protons with the radiation field of the source [10]. This upper bound implies a diffuse neutrino flux of $\sim 20/\mathrm{km}^2/\mathrm{year}$ (in 4π sr) in the energy range above 100 TeV.

The rate predicted in reference [10] is very low for ANTARES, which has a detector area of 0.1 km^2 and an angular acceptance of 2π sr. Nevertheless, a significantly higher event rate can be obtained by lowering the energy threshold to around 100 GeV. The background is greatly reduced by requiring a spatial and temporal coincidence with an observed GRB, offering a unique opportunity for high energy neutrino detectors to observe neutrinos associated with individual bursts.

2.1.5 Relic sources

In recent years, the Fly's Eye atmospheric fluorescence detector and the AGASA air shower array have convincingly detected [15] cosmic rays with energies exceeding $\sim 5 \times 10^{19}$ eV — the Greisen-Zatsepin-Kuz'min (GZK) cutoff set by interactions on the 2.7 K black body cosmic microwave background. These ultra high-energy cosmic rays (UHECR) constitute a population distinct from those at lower energies ($< 5 \times 10^{18}$ eV), in having a flatter spectrum. The depth in the atmosphere at which the shower reaches its maximum suggests a correlated change in the composition from iron nuclei to protons between 10^{18} and 10^{19} eV [16]. The lack of any detectable anisotropy argues against a local origin in the Galactic disc where the presumed sources of low energy cosmic rays reside. However, there are no potential extra-galactic sources such as active galaxies near enough (within $\sim$ 50 Mpc) to evade the GZK cutoff. Thus the origin of the UHECR is a major puzzle for standard physics and astrophysics.

An exciting possibility is that UHECRs result from the decay of massive particles, rather than being accelerated up from low energies. The most popular models in this context are based on the annihilation or collapse of topological defects (TDs) such as cosmic strings or monopoles formed in the early universe [17]. When TDs are destroyed, their energy is released as massive gauge and Higgs bosons with masses of $\mathcal{O}(10^{25})$ eV if such defects have formed at the GUT-symmetry breaking phase transition. The decays of these bosons can generate cascades of high energy nucleons, γ-

rays and neutrinos. These models are constrained both by considerations of the cosmological evolution of TDs [18] and observational bounds on the extra-galactic γ-ray background [19]. These require the mass of the decaying bosons to be less than $\sim 10^{21}$ eV, i.e. well below the GUT scale. Since only GUT scale TDs have independent motivation, e.g. to provide 'seeds' for the formation of large-scale structure, the above constraint thus disfavours TDs as the source of UHECRs.

A more recent suggestion is that UHECRs arise from the decays of metastable relics with masses exceeding $\sim 10^{21}$ eV which constitute a fraction of the dark matter [20, 21]. Such particles can be naturally produced with a cosmologically-interesting abundance during re-heating following inflation [22]. A lifetime exceeding the age of the universe is natural if they have only gravitational interactions, e.g. if they are 'cryptons' — bound states from the hidden sector of string theory [23, 21]. This interpretation also naturally accounts for the required mass. A detailed study of the fragmentation of such heavy particles has been performed [21] in order to calculate the expected spectra of nucleons, γ-rays and neutrinos. Such particles would, like all 'cold dark matter' particles, be strongly clustered in the Galactic halo, i.e. within $\sim$ 100 kpc. Therefore, the extra-galactic contribution to the cosmic ray flux would be negligible in comparison and the observed flux fixes the ratio of the halo density to the lifetime. As an example, if such particles comprise all of the halo dark matter then the required lifetime is $\sim 10^{20}$ yr, with a proportionally shorter lifetime for a smaller contribution.

Most of the energy in the cascade ends up as neutrinos and the predicted flux is then $F(> E_\nu) \approx 10^8 (E_\nu/1\ TeV)^{-1}$ km^{-2}y^{-1}sr^{-1}, through normalisation to the observed UHECR flux. Furthermore, the neutrinos should be well correlated in both time and arrival direction with the UHECRs, given the relatively short propagation length in the halo. A small departure from isotropy of $\mathcal{O}(20\%)$ should also be observed, since our location is $\sim$ 8 kpc from the galactic centre [24]. This anisotropy will be less than that for UHECRs, however, since there is no GZK cutoff to reduce the extra-galactic (isotropic) flux of neutrinos [25].

The essential point is that *whatever* process creates the UHECRs, it is exceedingly likely that there is a concomitant production of very high energy neutrinos. Measurement of the neutrino flux will, at the very least, provide important clues as to the origin of UHECRs and may even provide dramatic evidence for new physics.

2.2 Neutrino oscillations

The observation of atmospheric neutrinos with a neutrino telescope provides a means to study neutrino oscillations with a base-line length up to the order of the diameter of the Earth. The focus of investigation is the muon neutrino, but there is also a very interesting possible signature for extremely high energy (> 100 TeV) tau neutrinos.

2.2.1 Atmospheric ν_μ oscillations

Atmospheric neutrinos are emitted in the decay of hadrons produced by the interactions of cosmic rays with atmospheric nuclei. The production of electron neutrinos and of muon neutrinos is dominated by the processes $\pi^\pm \rightarrow \mu^\pm + \nu_\mu/\overline{\nu}_\mu$ followed by $\mu^\pm \rightarrow e^\pm + \overline{\nu}_\mu/\nu_\mu + \nu_e/\overline{\nu}_e$. In an infinite medium the ratio, r, of the flux of ν_μ and $\overline{\nu}_\mu$ to the flux of ν_e and $\overline{\nu}_e$ is expected to be two. Since the atmosphere is not an infinite medium, this ratio increases with increasing neutrino energy, because not all high energy muons can decay before they are absorbed by the ground. Furthermore, the magnetic field of the Earth has some influence on low energy charged particles and this modifies the energy spectra below a few GeV.

These effects are taken into account for the calculations of the predicted neutrino fluxes. The overall normalisation uncertainty is estimated to be about 20%, which is due to systematic theoretical uncertainties in the energy spectra of the primary cosmic rays and to the uncertainties in their composition. Generally, experimental results are reported as $R = r_{\mathrm{DATA}}/r_{\mathrm{MC}}$ in order to cancel common systematic uncertainties thereby reducing the overall uncertainty in R to about 5%.

Measurements published by underground experiments [26, 27, 28, 29] show evidence of a deficit in the number of muon neutrinos with respect to electron neutrinos. No anomaly was observed by the Fréjus [30, 31] and NUSEX [32] experiments.

Neutrino oscillations have been proposed as an explanation for the low value of the ratio R. With the hypothesis of two-neutrino mixing, the oscillation probability is:

$$P = \sin^2 2\theta \sin^2 \left(1.27 \frac{L}{E} \Delta m^2\right)$$

where θ is the mixing angle, L is the distance travelled by the neutrino (in km), E is the neutrino energy (in GeV) and Δm^2 is the difference of the square of the masses (in eV^2). As the neutrinos are produced in the atmosphere, the distance L ranges between 15 km, for vertically downward-going neutrinos, and almost 13 000 km, for vertically upward-going neutrinos.

A recent analysis [28] reported by the Super-Kamiokande collaboration outlines evidence for $\nu_\mu \leftrightarrow \nu_x$, where ν_x may be ν_τ or a "sterile" neutrino, with $\sin^2 2\theta > 0.82$ and $10^{-3} < \Delta m^2 < 8 \times 10^{-3}\,\mathrm{eV}^2$ at 90% confidence level. The most probable solution is $\Delta m^2 = 3.5 \times 10^{-3}\mathrm{eV}^2$ and $\sin^2 2\theta = 1.0$ (maximum mixing). Given these values, the survival probability $1 - P$ vanishes for $L/E = (2n+1) \times 353$ km GeV^{-1}, where n is a non-negative integer. Figure 2.1 shows the variation of the survival probability as a function of L/E.

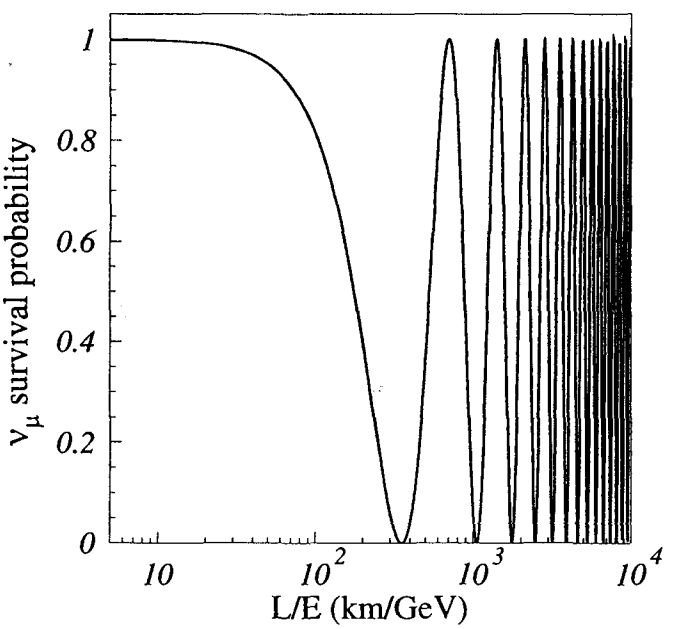

Figure 2.1: Variation of the neutrino survival probability as a function of L/E for $\Delta m^2 = 3.5 \times 10^{-3}\mathrm{eV}^2$ and maximal mixing.

Several points remain to be clarified. First of all, there are three

different regions of Δm^2 which have been explored with solar neutrinos, atmospheric neutrinos and short baseline beam neutrinos respectively, all of which indicate evidence of non-zero Δm^2. This cannot be supported in a three-flavour neutrino scheme. Moreover, the present result found in the Super-Kamiokande experiment is only marginally compatible with the result of Kamiokande [26] ($\Delta m^2 = 1.8 \times 10^{-2}$) and is in disagreement with the analysis of stopping upward-going muons performed by the IMB collaboration [33] which excluded the region presently favoured by Super-Kamiokande on the $(\sin^2 2\theta, \Delta m^2)$ diagram. The results reported by the Fréjus [30] experiment exclude the region $\Delta m^2 > 4 \times 10^{-3}\,\mathrm{eV}^2$ at 90% confidence level.

An independent measurement of the region $60 < L/E < 1250\,\mathrm{km/GeV}$ could resolve the uncertainties in the interpretation of these different experiments. This region contains the principal oscillation (first dip) for the Δm^2 values in question: $1 \times 10^{-3} < \Delta m^2 < 2 \times 10^{-2}\ \mathrm{eV}^2$. ANTARES is perfectly suited to this task. The peak sensitivity of the ANTARES detector is very near the most probable value reported by Super-Kamiokande. Accurate measurement of the position of the principal oscillation would provide a precise measurement of Δm^2.

Determination of the neutrino survival probability shown in figure 2.1 requires a measurement of the energy of the incident muon neutrino. For the isotropic νq and $\overline{\nu q}$ charged-current interactions, half of the neutrino energy goes to the hadron shower. For the $\bar{\nu} q$ and $\nu \bar{q}$ interactions, a much larger fraction of the energy goes to the muon, but these interactions are three times less frequent than the isotropic interactions. The energy of the hadron showers is difficult to estimate accurately, so the measurement of the oscillation parameters in ANTARES depends principally on the measurement of the muon momentum. The energy of the muon is determined by its range and the precision depends on the vertical spacing of the PMTs. The scale is set by the energy loss for vertical muons between groups of PMTs: 2 GeV for a vertical spacing of 8 m, and 4 GeV for a spacing of 16 m. Reconstruction inefficiencies degrade the energy resolution in an energy-dependent way, depending on the reconstruction algorithms employed. The current status of the reconstruction effort is described in chapter 6.

2.2.2 Tau neutrinos

Although the contribution of tau neutrinos to the atmospheric neutrino flux is negligible, their interactions must be taken into account when studying neutrino oscillations. If oscillations of the type $\nu_\mu \rightarrow \nu_\tau$ occur, the charged current interactions of ν_τ will produce charged τ leptons that can contribute to the signal observed. Most of the hadronic and electronic τ decays will escape detection, but the muonic decays $\tau^- \rightarrow \mu^- \bar{\nu}_\mu \nu_\tau$ can be seen in the ANTARES detector, and these events might be mis-identified as ν_μ interactions.

The muonic branching ratio of the τ is 17%. Furthermore, the charged-current interactions are considerably suppressed by the limited phase space due to the mass of the τ (1.78 GeV). For very large Δm^2 (1 eV^2), the number of ν_τ would be equal to the number of ν_μ over the entire atmospheric flux ($\leq$ 500 GeV), but the number of $\tau^-(\tau^+)$ produced with energies above 10 GeV would be only 53% (64%) of the number of $\mu^-(\mu^+)$ because of the limited phase space, and the contamination of the muon sample due to tau decays would be about 9% (11%). For smaller values of Δm^2, the contamination in the region of the main oscillation dip could be larger.

In [34] an attractive possibility for detecting very high energy neutrinos is proposed. The Earth is nearly transparent to low-energy neutrinos, but opaque to neutrinos above 100 TeV. Nonetheless, tau neutrinos well above 100 TeV can produce a signal in ANTARES because, unlike the $e^\pm$ and $\mu^\pm$ produced in ν_e and ν_μ interactions, the $\tau^\pm$ produced in ν_τ interactions decay before they are absorbed, producing ν_τ of lower energy which continue along the original ν_τ flight path, but with decreasing interaction probability. Once the ν_τ energy has been degraded to about 100 TeV, the ν_τ can penetrate the Earth and produce an accumulation of very-high-energy events in the detector. Such an accumulation would be a signal for tau neutrinos. Moreover, the flux of ν_τ from a given source would be constant during the Earth's rotation, whereas the flux of ν_μ would vary with the sidereal day because of the change in elevation seen from ANTARES. The variation of the ν_μ flux could not be observed from AMANDA, because it is located at the South Pole. A comparison of signals from the same sources observed at the different elevations corresponding to AMANDA and ANTARES could lead to very exciting results.

2.3 Indirect detection of neutralinos

2.3.1 Neutralinos as dark matter candidates

There is extensive astrophysical evidence [35] that most of the matter in the universe is non-luminous. The matter content of the universe is normally described in terms of the density parameter $\Omega = \rho/\rho_c$, where $\rho_c = 3H_0^2/8\pi G$ is the critical density and H_0, often expressed in the dimensionless form $h = H_0/100$ km s^{-1} Mpc^{-1}, is the expansion rate. Estimates of galactic halo masses from rotation curves and of the galactic number density give a value of $\Omega \geq 0.1$, whereas the luminous matter in galaxies corresponds to $\Omega < 0.01$. Studies of the dynamics of clusters and superclusters of galaxies increase the required value of Ω to around 0.2–0.3, and the popular inflationary paradigm generally requires $\Omega = 1$ (although this may include a contribution from a non-zero cosmological constant).

The density of baryonic matter is constrained by the abundances of the light elements to a range $0.008 \leq \Omega_{\rm baryons}h^2 \leq 0.024$. With current measurements of h tending to lie in the range 0.6–0.7, this indicates that much of the dark matter required on the galactic scale and beyond must be non-baryonic. A prime candidate for non-baryonic dark matter is the Lightest Supersymmetric Particle (LSP).

Supersymmetry is a spontaneously broken symmetry between bosons and fermions, postulated as a natural mechanism for avoiding GUT-scale radiative corrections to the Higgs mass. The minimal supersymmetric model (MSSM) [36] contains boson partners for every fermion, fermionic partners for all known bosons, and two Higgs doublets. In order to match the experimental limit on proton decay, it is generally assumed that a multiplicative quantum number called R-parity is conserved: $R = +1$ for ordinary particles and -1 for their supersymmetric partners. The natural consequence of this is that the lightest supersymmetric particle is stable, having no R-conserving decay mode.

The MSSM has numerous free parameters (105 from the most general soft-breaking terms in addition to the 19 parameters of the Standard Model, reducing to seven if we make a number of standard — but not necessarily correct — assumptions about masses and mixing angles), and the identity of the LSP is not unambiguous. However, experimental limits rule out a charged LSP over a broad mass range [37], and it is therefore generally assumed that the LSP is the lightest of the four neutralinos, the mass eigenstates

corresponding to the superpartners of the photon, the Z and the two neutral Higgs bosons. The mixing which generates the mass eigenstates depends on the choice of SUSY parameters: the LSP, χ, can be anything from a nearly pure B-ino to a nearly pure higgsino [38]. The mass of the LSP is constrained from below by non-detection in LEP2, and from above by the requirement that supersymmetry fulfil its role of maintaining the mass hierarchy between the GUT scale and the electroweak scale.

Neutralinos produced in the early universe will fall out of equilibrium when the annihilation rate, $\langle \sigma_A v \rangle n_\chi$, falls below the expansion rate H. This condition leads to the estimate that

$$\Omega_\chi \simeq \frac{3 \times 10^{-27} \text{ cm}^3 \text{ s}^{-1}}{\langle \sigma_A v \rangle},$$

where $\langle \sigma_A v \rangle$ is the thermally averaged annihilation cross-section times the relative velocity. (Note that neutralinos are Majorana particles, $\bar{\chi} = \chi$.) If the masses of SUSY particles are close to the electroweak scale, the annihilation cross-section is of order $\alpha^2/(100 \text{ GeV})^2 \sim 10^{-25} \text{ cm}^3 \text{ s}^{-1}$, indicating that $\Omega_\chi \sim 1$ is a realistic possibility. This heuristic argument is confirmed by detailed calculations, which indicate that a neutralino LSP has a cosmologically significant relic abundance over large regions of the MSSM parameter space [38].

2.3.2 Neutralino detection

If neutralinos make up a significant fraction of the Galactic dark halo, they will accumulate in the core of bodies such as the Earth or the Sun [38, 39, 40] and in the Centre of our Galaxy [41]. A neutralino passing through such a body has a small but non-zero probability of scattering off a nucleus therein, so that its velocity after scattering is less than the escape velocity. Once this happens, repeated passages through the body will generate additional scatters and the neutralino will sink relatively rapidly to the centre. Equilibrium will be reached when the gain of neutralinos from capture is balanced by the loss from annihilation, $C = C_A N^2$ where C is the capture rate, N is the number of captured neutralinos. The quantity C_A depends on the WIMP annihilation cross-section and the WIMP distribution.

The capture rate C depends on the local halo mass density ρ_χ, the velocity dispersion of neutralinos in the halo $\bar{v}$, and the elastic scattering cross-section, which depends on the mass of the neutralino and on the effective volume and

chemical composition of the Sun or Earth. Representative values of ρ_χ and $\bar{v}$ are 0.3 GeV cm^{-3} and 270 km s^{-1} respectively. Jungman et al. [38] quote capture rates of

$$C_\odot = 2.4 \times 10^{37}\ \mathrm{s}^{-1} \frac{\rho_\chi}{0.3\ \mathrm{GeV\ cm}^{-3}} f_\odot(m_\chi) f_p(\mathrm{GeV}^2)^2,$$
$$C_\oplus = 2.4 \times 10^{28}\ \mathrm{s}^{-1} \frac{\rho_\chi}{0.3\ \mathrm{GeV\ cm}^{-3}} f_\oplus(m_\chi) f_p(\mathrm{GeV}^2)^2,$$

where f_p is the neutralino-nucleon scalar coupling and the dependence on the neutralino mass is given by $f_\odot$ and $f_\oplus$ for Sun and Earth respectively. For the Sun, $f_\odot$ is a smoothly varying function of mass, decreasing from $\mathcal{O}(5)$ at $m_\chi = 10$ GeV/c^2 to $\mathcal{O}(0.05)$ at 1 TeV/c^2; for the Earth, resonances occur whenever the neutralino mass equals the mass of the target nucleus, so there is a good deal of structure in $f_\oplus$ below $m_\chi = 100$ GeV/c^2, with a main resonance at 56 GeV (^{56}Fe).

The annihilation rate can be calculated [38, 40] from the thermally-averaged cross-section, $\langle \sigma_A v \rangle$, in the limit of zero relative velocity; at equilibrium it is simply half the capture rate. The time taken to reach equilibrium, $\tau = (CC_A)^{-1/2}$, is longer for the Earth than for the Sun: over a wide range of MSSM parameter space, the Earth's neutralino population has not yet reached equilibrium, and the observed annihilation rate will be suppressed by some model-dependent amount compared to the equilibrium rate.

2.3.3 Neutrinos from neutralino annihilation

Neutralinos annihilate into a fermion-antifermion pair or into various two-body combinations of W, Z and Higgs bosons [38, 40]. Direct decay into neutrinos is zero in the non-relativistic limit, but decays into c, b and t quarks, τ leptons, Z, W and Higgs can all produce a significant flux of high-energy neutrinos (light quarks and muon pairs do not contribute, as they are stopped before they decay). The typical neutrino energy produced is thus around one-half to one-third of the neutralino mass, with a broad spectrum whose detailed features depend on the branching ratios into the different channels (which in turn depend on the neutralino composition—gaugino vs higgsino—as well as its mass) and are modified, especially in the Sun, by hadronisation and stopping of c and b quarks, and stopping, absorption and possibly oscillation of neutrinos [38, 40, 42].

Since both the neutrino-nucleon cross-section and the range of the produced muon scale with the neutrino energy, the resulting muon rate is approximately proportional to $E_\nu^2 \, dN_\nu/dE_\nu$, indicating that this method of neutralino detection is most likely to be competitive for higher mass neutralinos.

The expected muon flux depends on the neutralino mass and the assumed MSSM parameters. The results of representative calculations [39] are shown in figure 2.2. In these models, the flux from the Sun exceeds that from the Earth at high neutralino masses (in others, e.g. [40], the solar flux is larger throughout). The exposure required to detect a signal (defined in [39] as a 4σ effect above background with at least 4 events) is of the order of 10^4 to 10^5 $m^2 \cdot yr$.

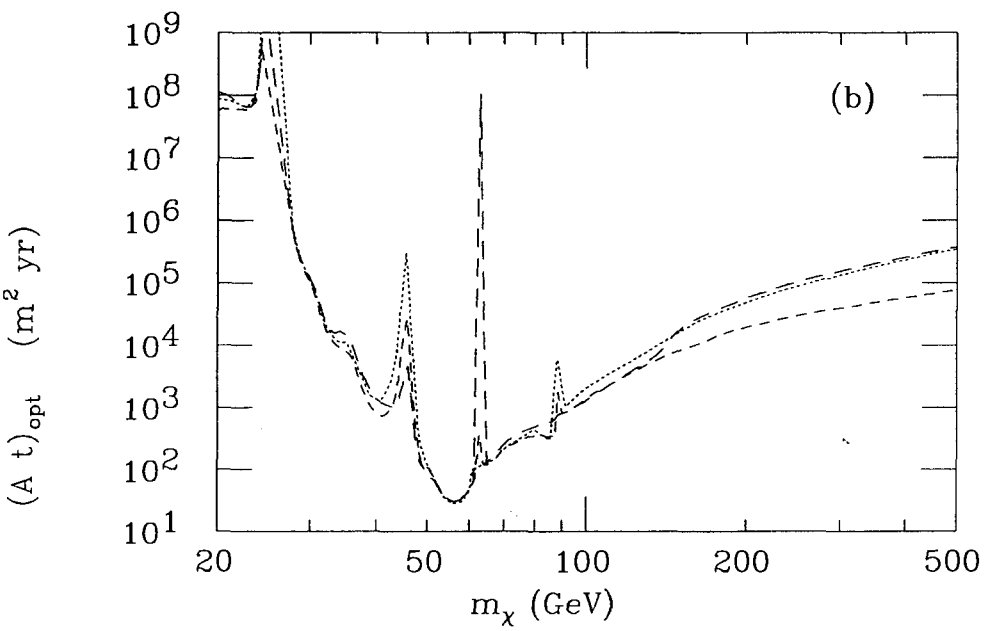

Figure 2.2: Exposure required to detect a neutralino signal. The figure is taken from Bottino et al. [39] and the 3 curves correspond to different choices of supersymmetry parameters.

The Sun is a point-like source of neutrinos from neutralino annihilation, but the Earth is not, especially for lower mass neutralinos. Despite the smearing produced by measuring the muon flux rather than the neutrinos, a detector with good angular resolution would be able to use the observed

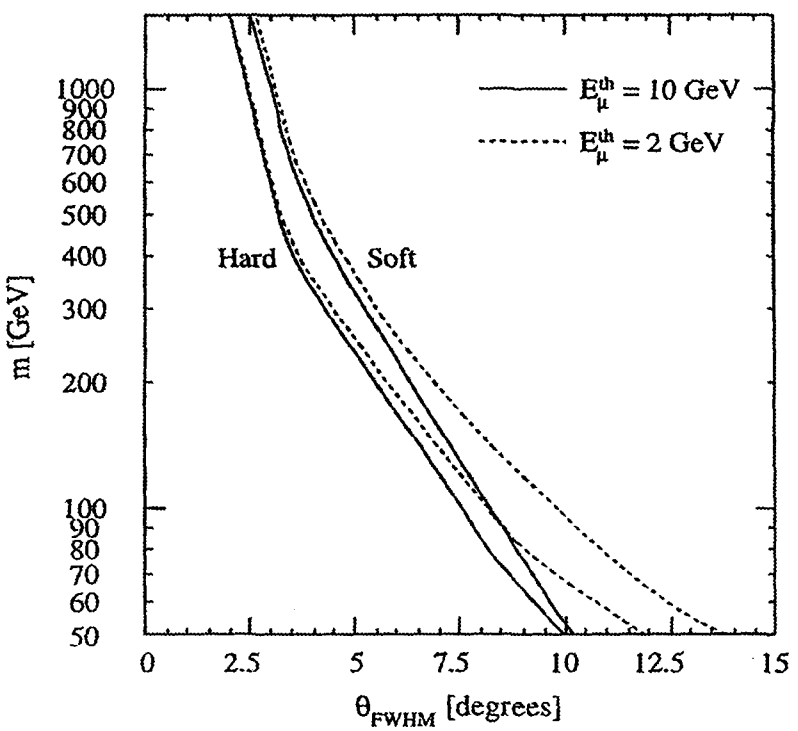

Figure 2.3: Mass of the neutralino versus expected angle for different supersymmetry parameters. The figure is taken from Edsjö [40].

angular distribution to constrain the neutralino mass, as shown in figure 2.3 from [40].

Indirect detection explores a region of parameter space which is somewhat different from that investigated by direct techniques, although there is also considerable overlap. Indirect detection is particularly useful when the axial coupling of the neutralino dominates [38], as axially-coupled neutralinos are captured in the Sun due to their interaction with hydrogen. Detection of neutralinos by both direct and indirect techniques would provide information on neutralino couplings and MSSM parameters, as would indirect detection of signals from both the Sun and the Earth.

2.4 Other exotic phenomena

2.4.1 GUT monopoles

Grand Unified Theories (GUT) of the electroweak and strong interactions predict the existence of massive magnetic monopoles. It is assumed that they were produced shortly after the Big Bang and would have cooled down to very low velocities ($\beta \leq 10^{-3}$). They may be at the origin of baryon number violating processes [43] and have been searched for in proton decay experiments.

The best limits to date are provided by the MACRO [44] and BAKSAN [45] experiments. In the region $10^{-4} \leq \beta \leq 10^{-3}$, they have achieved sensitivity below the Parker bound [46]. Baikal has obtained limits which could be comparable with a limited number of photomultipliers (36 and 192) [47]. A 1000 PMT detector could bring appreciable improvement on the results. ANTARES is studying a special trigger similar to that of Baikal. The slow moving monopole produces sequential Cherenkov flashes along its track via the proton decay products. The trigger is based on counting rate excesses during short time periods of 100 microseconds to 1 ms.

2.4.2 Relativistic monopoles

According to [48], the Ultra High Energy Cosmic Ray Events above 10^{20} eV may be relativistic monopoles. In this case, the basic mechanism for light generation is Cherenkov radiation. The intensity of the light due to relativistic monopoles is giant, similar to that of PeV muons, and they can be obtained with the muon trigger. Preliminary estimates [47] show that they can be distinguished from high energy muons, down to monopole velocities $\beta = 0.1$.

2.4.3 SUSY Q-balls

Supersymmetry predicts the existence of non-topological solitons, often called Q-balls. It has been realized that solitons with a large number of baryons are stable and can be produced copiously in the early Universe, which means that they are an interesting dark matter candidate [49]. The signature and rate of occurrence of a Q-ball through a detector depend on the parameters of the theory. In the case of large baryon numbers of the order of 10^{24},

emissions of the order of 10 GeV/mm are possible, a spectacular signature, similar to those expected from monopole searches [50].

2.4.4 New phenomena

Whenever a new window is opened on the Universe, unexpected phenomena are observed. This has been verified in numerous cases throughout history, from the observation of the moons of Jupiter by the first Galilean telescopes to the discovery of pulsars with radio-based astronomy. Neutrino astronomy provides an exciting new probe of the Universe to the highest possible redshifts in an energy window so far not observable by other techniques. There is plenty of scope for surprises.

This page is intentionally left blank.

Chapter 3

Detection principles

Since the Earth acts as a shield against all particles except neutrinos, a neutrino telescope uses the detection of upward-going muons as a signature of muon neutrino interactions in the matter below the detector. The muon detection medium may be a natural body of water or ice through which the muon emits Cherenkov light. Its detection allows the determination of the muon trajectory. This detection technique requires discriminating upward going muons against the much higher flux of downward atmospheric muons (figure 3.1). To simplify the discrimination, the detector should be installed in a deep site where a layer of water or ice would shield it.

In order to correlate the measured muon spectrum with the original neutrino spectrum, it is necessary to understand the dynamics of neutrino interactions, the opacity of the Earth, the energy loss of muons and the resolution of the detector over a wide range of angles and energies.

3.1 Neutrino interactions

The inclusive deep inelastic charged current cross-section for $\nu_l + N \rightarrow l^- + X$ (where the lepton mass is neglected) is given by [51]

$$\frac{d^2\sigma_{\nu N}}{dxdy} = \frac{2G_F^2 m_N E_\nu}{\pi} \frac{M_W^4}{(Q^2 + M_W^2)^2} \left[xq(x,Q^2) + x(1-y)^2\bar{q}(x,Q^2)\right]$$

where G_F is the Fermi constant, m_N and M_W are the nucleon and W-boson masses, and Q^2 is the square of the momentum transfer between the neutrino and muon. The Bjorken variables x and y are $x = Q^2/2m_N\nu$ and

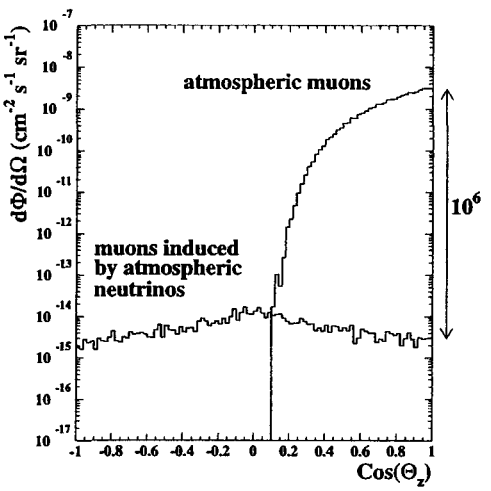

Figure 3.1: Zenith angular distribution of the muon flux above 1 TeV from atmospheric muons and atmospheric neutrino induced muons at 2300 m water equivalent depth.

$y = (E_\nu - E_l)/E_\nu$, where $\nu = E_\nu - E_l$ is the lepton energy loss in the laboratory frame.

3.1.1 Interactions at low energies

At energies such that $E_\nu \ll M_W^2/2m_N \approx 5$ TeV, Q^2 can be neglected in the W propagator. In this case the average deep-inelastic νN cross-sections grow linearly with the neutrino energy (see figure 3.2):

$$\sigma_{DIS}(\nu N) \simeq 0.67 \times 10^{-38} E_\nu[\text{GeV}] \text{ cm}^2$$
$$\sigma_{DIS}(\bar{\nu} N) \simeq 0.34 \times 10^{-38} E_\nu[\text{GeV}] \text{ cm}^2$$

At even lower energies ($E_\nu < 100$ GeV), quasi-elastic and resonant contributions to the charged-current interactions have to be considered. In this case Q^2 has to be small enough to allow a coherent interaction with the complete target nucleon, so these cross-sections are essentially constant with energy. A fit to data above 10 GeV gives the following sums for the quasi-elastic and resonant production processes [52]:

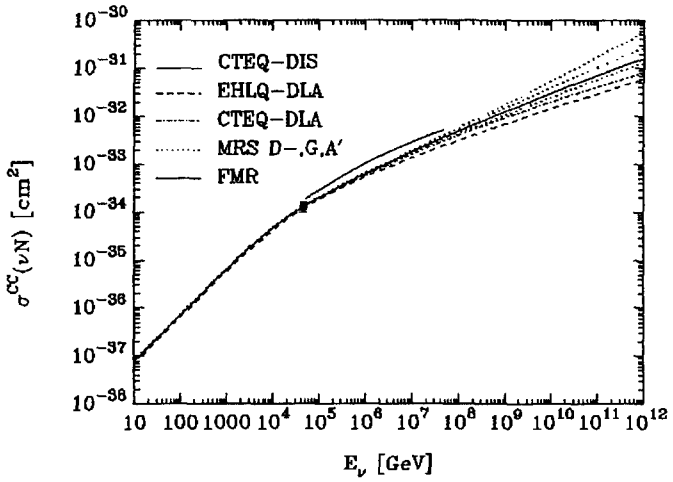

Figure 3.2: Average charged-current cross-section for ν-N interactions for different sets of parton distribution functions. The data point corresponds to the average of the measurements by H1 and ZEUS at HERA (taken from [51]).

$$\sigma_{QE}(\nu_\mu N) + \sigma_{res}(\nu_\mu N) = 1.50 \times 10^{-38}\,\mathrm{cm}^2$$
$$\sigma_{QE}(\bar{\nu}_\mu N) + \sigma_{res}(\bar{\nu}_\mu N) = 1.58 \times 10^{-38}\,\mathrm{cm}^2$$

Between 10 GeV and 500 GeV the vertical ν_μ flux is approximately proportional to $1/E_\nu^3$. Integrating the cross-sections given above over this flux for $E_\nu > 10$ GeV results in a quasi-elastic and resonant contribution of 11% for ν_μ and 21% for $\bar{\nu}_\mu$ interactions.

3.1.2 Interactions at high energies

At energies such that $E_\nu \gg M_W^2/2m_N \approx 5$ TeV, quasi-elastic and resonant contributions are completely negligible. On the other hand, the W propagator limits the growth of Q^2 to $\langle Q^2 \rangle \sim M_W^2$ and so the cross-section is dominated by the behaviour of distribution functions at small x.

The H1 and ZEUS collaborations at HERA measured the proton structure function $F_2(x, Q^2)$ via charged current $e - p$ scattering, for Q^2 in the range from 1.5 to 5000 GeV^2 with x down to 3×10^{-5} at $Q^2 = 1.5$ GeV^2 and x down to 2×10^{-2} at $Q^2 = 5000$ GeV^2 [53].

These measurements can be translated into a neutrino-nucleon interaction cross-section at $E_\nu \simeq 50$ TeV and can also be used as a guide to extrapolate the parton densities beyond the measured ranges in x and Q^2 to those required for higher neutrino energies. Figure 3.2 shows the behaviour of the average νN cross-section for different sets of parton distribution functions. At very high energy, the cross-section calculated with the new parton distribution functions (CTEQ3-DIS [54]) is more than a factor of 2 larger than previous estimates.

3.1.3 Different types of ν interactions in ANTARES

Charged-current ν_e interactions give rise to electromagnetic and hadronic showers with longitudinal dimensions of no more than a few metres, because the radiation length and the nuclear interaction length of water are below 1 m. On the scale of ANTARES, these are nearly point-like events. At energies above 100 GeV, the energy resolution of these events is expected to be better than for muonic events because they leave all of their energy inside the detector volume. On the other hand, their angular resolution will be poor compared to muonic events, due to the point-like character of the showers.

Charged-current ν_e interactions will be contaminated by neutral-current interactions of both ν_e and ν_μ (and ν_τ, if present). The number of neutral-current interactions is about 1/3 of the number of charged-current interactions. The neutrino type is not identified in the neutral-current interactions, the energy resolution is poor due to the missing final-state neutrino, and the angular resolution is poor due to the point-like character.

Charged-current ν_μ interactions produce $\mu^\pm$ leptons as well as a point-like hadronic shower. The ν_μ energy can be estimated from the measured $\mu^\pm$ energy. In $\nu_\mu d \rightarrow \mu^- u$ interactions, the average μ^- energy is 1/2 of the ν_μ energy; in $\bar{\nu}_\mu u \rightarrow \mu^+ d$ interactions, the average μ^+ energy is 3/4 of the $\bar{\nu}_\mu$ energy. The $\mu^\pm$ energy can be determined from the range for $E_\mu < 100$ GeV, or from dE/dx for $E_\mu > 1$ TeV (see below). For ν_μ interactions inside the detector, additional information on the ν_μ energy is available from the hadronic shower. The ANTARES detector is designed for the detection of these charged-current ν_μ interactions.

Charged-current ν_τ interactions produce $\tau^\pm$ leptons with electronic, muonic and hadronic decay modes. The ν_τ interaction vertex and the $\tau^\pm$ decay vertex cannot be separated for energies below $\sim$100 TeV. The

electronic and hadronic modes will look like ν_e charged-current or neutral-current interactions. The muonic decays $\tau^- \rightarrow \mu^- \bar{\nu}_\mu \nu_\tau$, with branching ratio 17%, will be visible in ANTARES, but they cannot be distinguished from ν_μ interactions.

3.2 Cherenkov light emission

Charged particles emit light under a characteristic angle when passing through a medium if their velocity exceeds the speed of light in the medium. The Cherenkov angle θ is related to the particle velocity β and the refractive index of the medium n:

$$\cos\theta = 1/n\beta$$

In the energy range interesting for ANTARES ($E > 10$ GeV), particles will generally be ultra-relativistic with $\beta = 1$. The refractive index of sea water is $n = 1.35$ for a wavelength of 450 nm therefore the Cherenkov light is emitted under 42° for this wavelength. This easy geometrical pattern of light emission allows a precise reconstruction of tracks from the measurement of only few hits at different space points.

The number of photons produced along a flight path dx in a wave length bin $d\lambda$ for a particle carrying unit charge is

$$\frac{d^2N}{d\lambda dx} = 2\pi\alpha \sin^2\theta/\lambda^2$$

At wavelengths of 400-500 nm the efficiency of the photomultipliers as well as the transparency of the water are maximal. Within 1 cm flight path 100 photons are emitted in this wavelength bin. Between 285-400 nm twice as many photons are emitted, however they contribute less to the detected signal. At a perpendicular distance of 40 m from a charged track the density of photons between 400-500 nm is still 1 per 340 cm^2, neglecting absorption and scattering effects. The effective area of the photomultipliers being considered is in the same range (300-500 cm^2). This gives an indication of the active detector volume around each photomultiplier.

For $\beta = 1$ the Cherenkov light yield is independent of the energy of the charged particle. This means the light output of a single particle does not allow its energy to be measured. However when hadronic or electromagnetic showers are produced (which might occur at the neutrino vertex as well as

for radiative processes along a muon track) the total light yield of the shower will be proportional to the total track length in the shower and therefore to its initial energy. This allows some calorimetric measurements if the neutrino vertex is inside the active detector volume or for muon tracks above 1 TeV where radiative processes dominate its energy loss.

3.3 Light propagation in sea water

The processes of absorption and scattering characterise the transmission of light in water. They are parametrised by the absorption length λ_a, the scattering length λ_s, and the scattering function $\beta(\theta)$ which describes the angular distribution of the scattering [55]. The relevant window of wavelengths for a sea water Cherenkov detector is centred on blue light. Deep sea water transparency is maximal in the blue, with typical values of 60 m for λ_a and λ_s, and a scattering function peaked in the forward direction with an average value for the cosine of the scattering angle $\langle\cos(\theta)\rangle \simeq 0.9$, as shown in figure 3.3 taken from [55]. Seasonal variations are expected to affect these values, especially the scattering parameters which are governed by the amount of suspended particulate matter. In section 4.2.3 we present results of *in situ* measurements of optical properties at the ANTARES site.

3.4 Detector response

The physical processes involved in neutrino and muon interactions place limits on the angular and energy resolution possible with a neutrino telescope. These limits must be taken into consideration when optimising the detector design.

3.4.1 Angular response for ν_μ interactions

The angular response of the detector with respect to the incoming neutrino direction is crucial for the identification of point sources of neutrinos. Three factors determine this response: the angle between the neutrino and the muon in the neutrino interaction, the deviation of the muon direction due to multiple scattering and the angular resolution of the detector with respect to the muon.

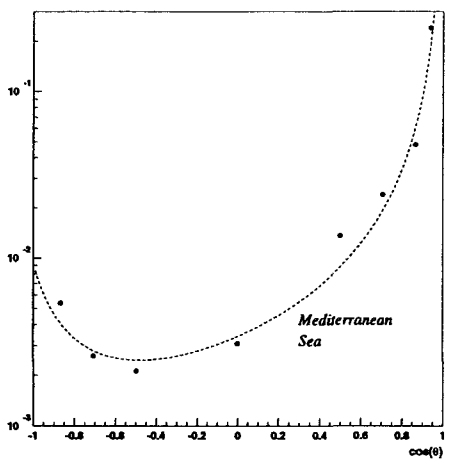

Figure 3.3: The angular distribution of scattering in the deep Mediterranean Sea [55].

The effect of the first two factors is illustrated in figure 3.4. At 1 TeV the average difference between the ν direction and the μ is about 0.7°. The difference decreases with increasing ν energy.

The detector resolution will be determined by the quality of the alignment of the detector components, the time resolution of the photomultipliers, the global timing of the readout system and the quality of the muon reconstruction. The reconstruction will be affected by light coming from secondary particles and by scattered light. Monte Carlo studies show that an angular resolution of 0.1° is possible. This means that above 100 TeV the total angular resolution is dominated by detector effects whereas below 10 TeV the resolution is dominated by the angular distribution of the neutrino interactions.

3.4.2 Energy response for ν_μ interactions

The energy response is determined by the energy fraction transferred to the muon in the neutrino interaction, the energy lost by the muon outside the detector and the energy resolution of the detector. The muon energy determination requires different techniques in different energy ranges.

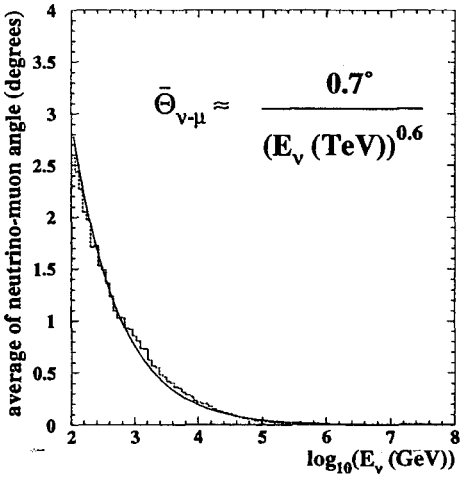

Figure 3.4: Angular difference between the initial neutrino direction and that of the muon track at the detector; the functional form shown reproduces the observed energy dependence well (solid curve).

Below 100 GeV, the muons are close to minimum-ionizing, and the energy of contained events, with start and end points measured inside the detector, can be determined accurately from the range. The threshold for this method is about 5-10 GeV for vertical tracks, depending on the vertical distance between groups of optical modules, and about 15 GeV for more isotropic events, depending on the horizontal distance between lines.

Above 100 GeV, the range cannot be measured because of the limited size of the detector, but the visible range determines a minimum energy that can be used for the analysis of partially-contained events: starting events in which the vertex point is measured inside the detector, and stopping events in which the endpoint is measured.

Above 1 TeV, stochastic processes (bremsstrahlung, pair production, δ-rays) are dominant, and the muon energy loss becomes proportional to the energy. The muon range above 1 TeV increases only logarithmically with the muon energy (figure 3.5). On the other hand, the detection efficiency increases with energy because of the additional energy loss. The correlation between measured muon energy and neutrino energy is shown in figure 3.6. Monte Carlo studies have shown that the neutrino energy can be determined

within a factor 3 above 1 TeV from the average energy loss.

Above 1 PeV, the Earth becomes opaque to upward-going vertical neutrinos. Higher energies are accessible closer to the horizon, however. Very high-energy tau neutrinos can be observed because the $\tau^{\pm}$ produced in ν_τ interactions decay before they are absorbed, producing ν_τ of lower energy which continue along the original ν_τ flight path, but with decreasing interaction probability, resulting in an accumulation of events at the highest detectable energies.

3.5 Observable sky

The ANTARES neutrino telescope, situated at a latitude of 43° North, can observe upward-going neutrinos from most of the sky (about 3.5π sr), due to the rotation of the Earth. Declinations below $-47°$ are always visible, while those above $+47°$ are never visible. Declinations between $-47°$ and $+47°$ are visible for part of the sidereal day (figure 3.7). Most of the Galactic plane is visible, and the Galactic centre is visible most of the sidereal day. Since the AMANDA telescope at the South pole is sensitive to positive declinations, the two detectors will have a reasonable area in common for cross-checks (about 1.5π sr).

At energies greater than $\simeq$ 40 TeV, the interaction length becomes smaller than the Earth's diameter for ν_μ traversing the dense core of the Earth. Above 10 PeV, only nearly horizontal ν_μ are visible (see figure 3.8). If the field of view can be extended to 10° above the horizon at these energies where the background is greatly diminished, a non-negligible fraction of the sky can be kept observable even at these energies.

Like other underground detectors, neutrino telescopes can observe the sky independently of the time of day, the phases of the moon or the weather. Existing underground experiments have usually reached 80% duty cycle after the initial debugging phase. ANTARES aims for even higher values for the off-shore facilities because the access is complicated and time-consuming.

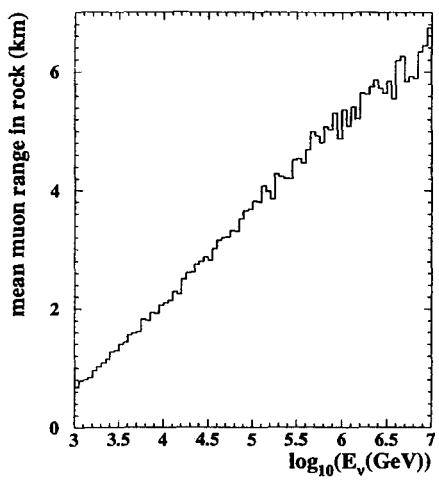

Figure 3.5: Average range of the muon in standard rock as a function of the initial neutrino energy.

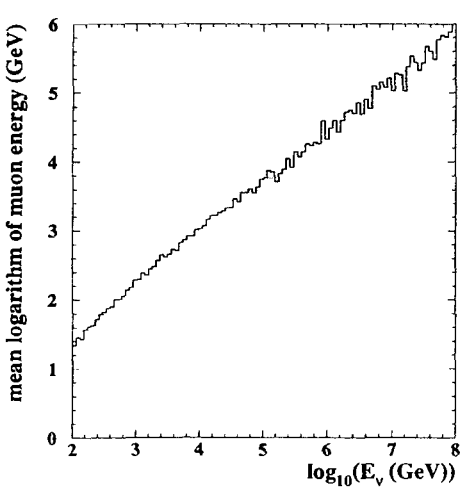

Figure 3.6: Muon energy at the detector as a function of the parent neutrino energy.

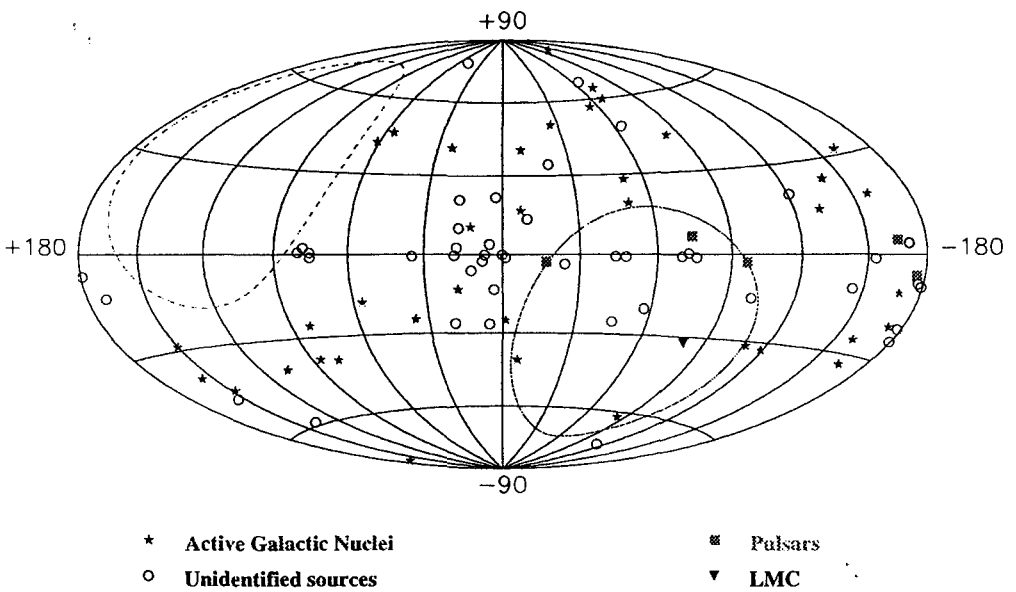

Figure 3.7: Visible sky in Galactic coordinates for a detector situated at 43° North latitude. The area within the dashed line is not observable; the area within the solid line is observable 24 hours a day. The sources shown are from the EGRET catalogue.

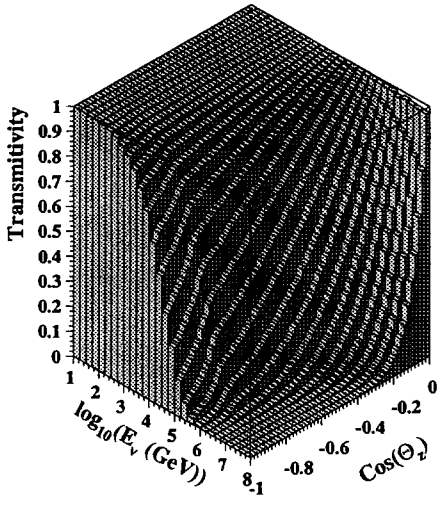

Figure 3.8: Transmittivity of the Earth as a function of incoming neutrino energy and zenith angle.

Chapter 4

R & D programme

In order to ensure the success of the deployment of a large-scale detector in an uncontrollable environment such as the deep sea, it is necessary to perform an extensive programme of site evaluation and prototype testing.

The selection of a suitable site for a neutrino telescope requires consideration of water transparency, optical background, fouling of optical surfaces, strength of the deep sea currents, meteorological conditions, depth, on-shore support, infrastructure and pier availability. This chapter reports on the results of site evaluation studies for the proposed site and on initial experience of prototype string construction and deployment.

4.1 Site evaluation mooring lines

A detailed programme of *in situ* measurements has been undertaken since October 1996, most of the data being taken at a site near Toulon (42°50' N, 6°10' E) at a depth of 2400 m (figure 4.1). Optical background data were also taken 20 nautical miles off Porto, Corsica (42°22' N, 8°15' E) at a depth of 2700 m.

Autonomous mooring lines to measure the site parameters have been developed and about 20 deployments and recoveries have been successfully performed. Three generic test lines exist, as illustrated in figure 4.2. Each test setup is incorporated in a mooring line anchored at the sea bed and vertically supported by a buoy. The measuring system, which can be up to 50 m long, is placed around 100 m above the sea bed. A further 30 m of cable and instrumentation sits between the measuring system and the top of the

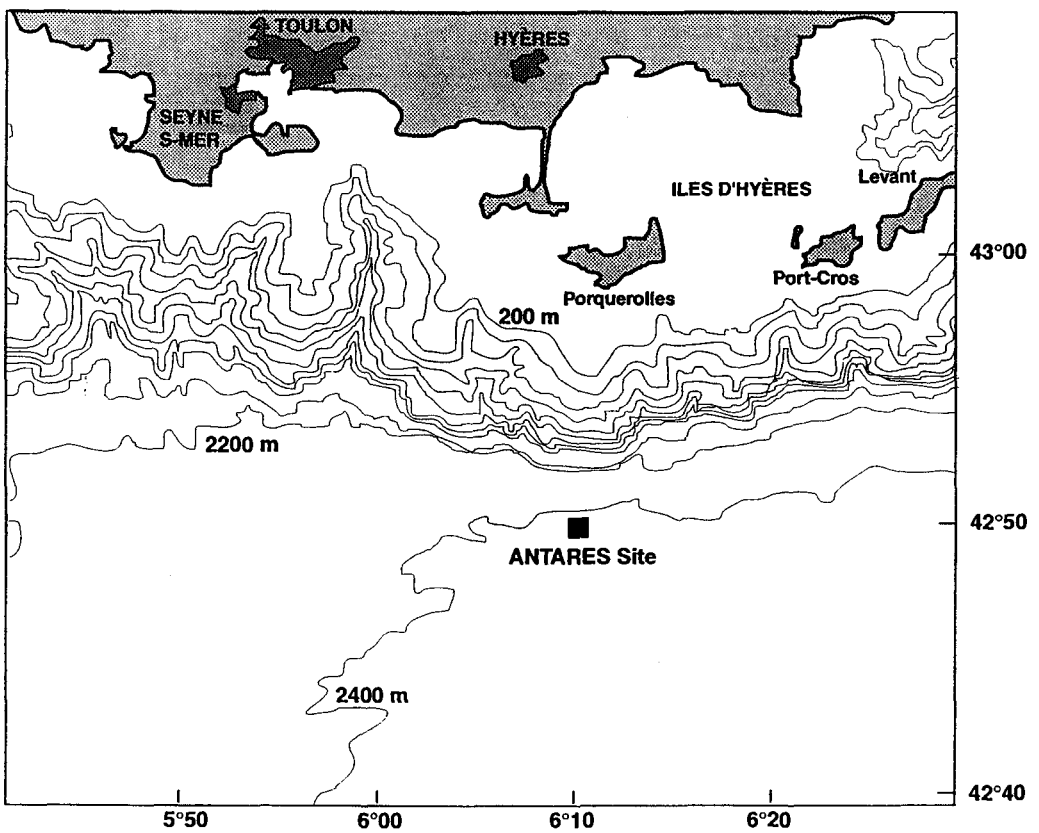

Figure 4.1: Map of the ANTARES site near Toulon.

test line. The electronics, data acquisition and the detectors are powered by a set of lithium battery packs. A 500 cm^3 pack delivers 8 A-h at 26 V. These compact power sources have a lifetime which permits stand-alone tests for periods as long as one year.

The test lines have been deployed using a standard horizontal deployment method. The buoy at the top of the line is immersed first, so that the line is held under tension during the entire operation. The boat continues to move slowly away from the buoy as the rest of the line is paid out from the boat. The anchor is the last element to be deployed after which the line falls to the sea bed.

To date, the measurements carried out confirm that the properties of this site satisfy the constraints of the ANTARES physics programme.

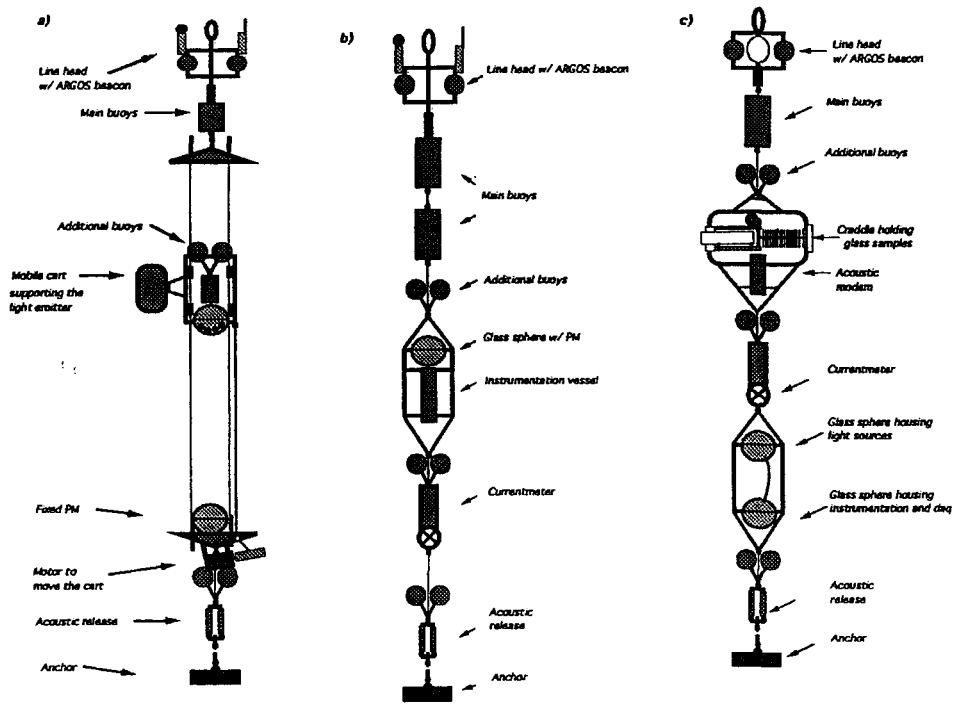

Figure 4.2: Test lines to study (a) light attenuation, (b) optical background, and (c) optical fouling.

It is planned to explore a wider area in the Mediterranean sea, for long periods, in order to study the variation of parameters as a function of site, depth and season. For specific parameters such as water transparency, measurements at several wavelengths are also foreseen. The results obtained so far have been instrumental in steering the design of the telescope.

4.2 Optical properties of the site

4.2.1 Optical background

The behaviour of the optical background on site places constraints on the trigger logic and the electronics as well as the mechanical layout of the optical modules. A setup has been devised for studying the time dependence of the

background as well as its spatial extent and its correlation with deep sea current. The relevant test line has been immersed ten times in total, for periods spanning from hours to months.

The optical modules used for these tests are similar to those discussed in detail in section 5.3. In this case 8-inch photomultiplier tubes were used.

Up to three optical modules have been used on the same line, two of which, A and B, were 0.5 m to 1.5 m apart, while the third, C, was 10 m to 40 m away. A current-meter was installed below the optical modules. Data consisted of measurements of singles rates for all three optical modules and coincidence rates for modules A and B within a time window of 100 ns. In order to sample long-term variations, the system was enabled for a few hours three times a week.

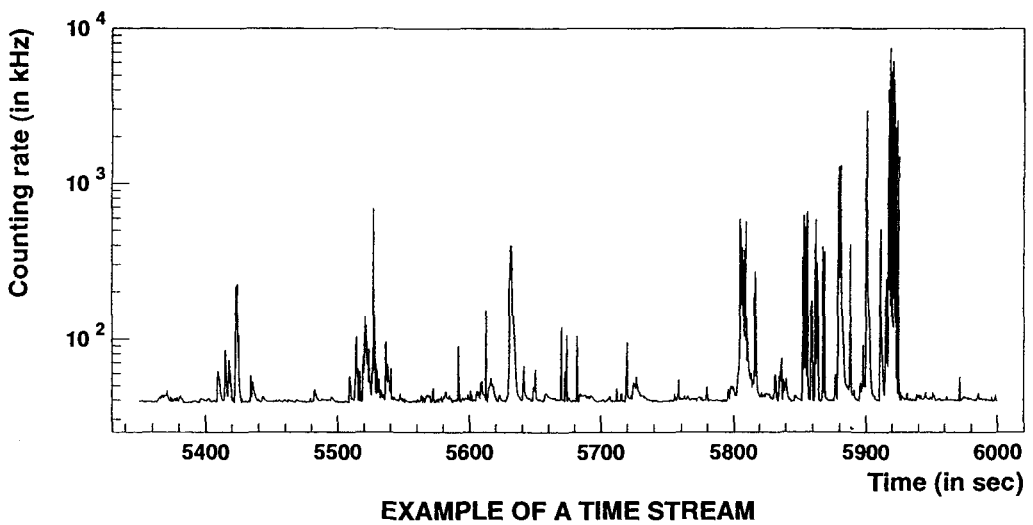

Figure 4.3: Time dependence of the counting rate.

An example of the observed counting rate is presented in figure 4.3 which exhibits two distinct components: a low level background around 40 kHz, and, superimposed on this, rapid ($\sim$ 1 s) excursions of up to several MHz. The low level background varies from 17 kHz to 47 kHz over a time scale of a few hours. This rate changes simultaneously on all optical modules even when they are 40 m apart. The peak activity is correlated with the current speed and is limited in spatial extent: peaks are seen simultaneously by optical modules when they are less than 1.5 m apart, but not when they

are more than 20 m apart. The dependence of bioluminescence activity on current velocity is emphasized in figure 4.4 where a correlation is observed between the two variables. This figure also illustrates evidence for site to site and seasonal variations in this correlation. However, further data are required to understand these effects.

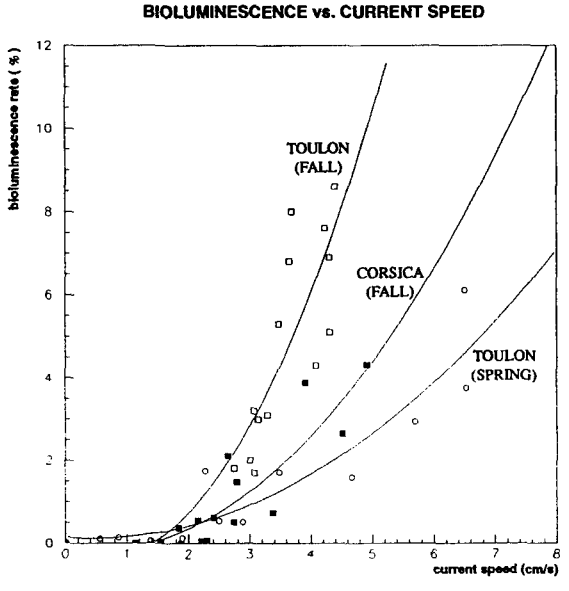

Figure 4.4: Bioluminescence burst activity as a function of current velocity. A parabolic fit is superimposed on the data.

4.2.2 Optical fouling

When exposed to sea water, the surfaces of optical modules are fouled by the combination of two processes: living organisms, mostly bacteria, grow on the outer surface, and sediments fall on the upward-looking surfaces. While the bacterial growth is expected to be almost transparent, sediments will adhere to it and make it gradually opaque, thus diminishing the sensitivity of the detector. This phenomenon is expected to be site-dependent as the bacterial growth decreases with depth and the sedimentation rate depends on local sources of sediments such as nearby rivers. A series of measurements has

been performed in order to quantify these phenomena.

Light of wavelength 470 nm from a blue LED source in a glass sphere was normally incident on a set of five PIN diodes placed at 50° to 90° from the vertical axis of the sphere inside a second sphere 1 m away. Measurements of the light transmission and current velocity were made twice daily.

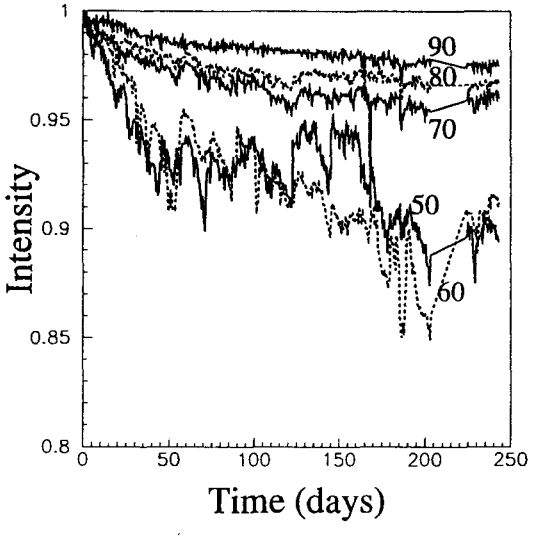

Figure 4.5: Light transmission as a function of time and polar angle.

Figure 4.5 shows the light transmission monitored for 240 days with this configuration. For the horizontally-looking PIN diode (90°), the light source is affected by the same fouling as the detector, thus doubling the effect. In this case, a transmission loss of 1.2% per surface is observed after 8 months of exposure. All optical modules in the ANTARES detector will point downward, reducing the loss even further.

In addition, a cradle holding glass slides mounted on a horizontal cylinder with various orientations around the axis of the cylinder (see figure 4.6) was incorporated into the mooring line. This apparatus was developed by IFREMER [56].

Two series of measurements have been performed with the apparatus being immersed for long periods (3 months and 8 months respectively)

at 2400 m depth on the same site as the other tests. After recovery, a biochemical analysis of the slides has been performed by several laboratories giving the results shown in figure 4.6. demonstrating the dependence of the biofouling on the orientation of the slides. In those cases, where the slides point downward, saturation is observed. According to marine biologists, these numbers are several orders of magnitude below what is observed at shallow depths.

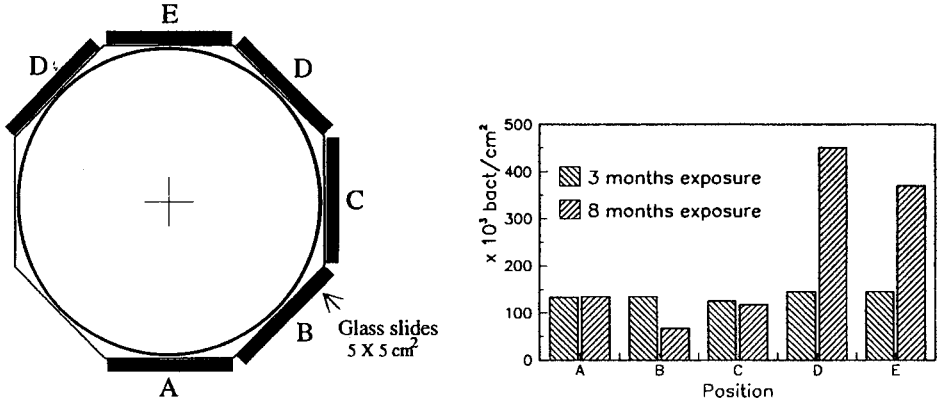

Figure 4.6: (left) Position of glass slides on cylinder, (right) number of deposited bacteria vs. cylinder position

The optical modules are housed in pressure-resistant glass spheres produced by the Benthos company. The mooring line which measured the fouling of Benthos spheres also included a sediment trap in order to determine the vertical flux and the composition of sediments at the ANTARES site. Particulate matter contributes to the scattering of light in sea water as well as the fouling of the Benthos spheres. The sediment trap collected samples from July to December 1997 on a weekly basis. The analysis of the samples was performed in the CEFREM (Centre de Formation et de Recherche sur l'Environnement Marin) laboratory by the team of Professor A. Monaco. As shown in figure 4.7, the total mass flux of sediments substantially increases from October onwards, probably as a result of heavy rainfall draining sediment from the shore. Indeed, the composition of the sediments shows a large contribution of material originating from continental river bed. This study will be complemented by the analysis of the sediment

cores and of the water samples collected during the ANTARES site survey campaign of December 1998.

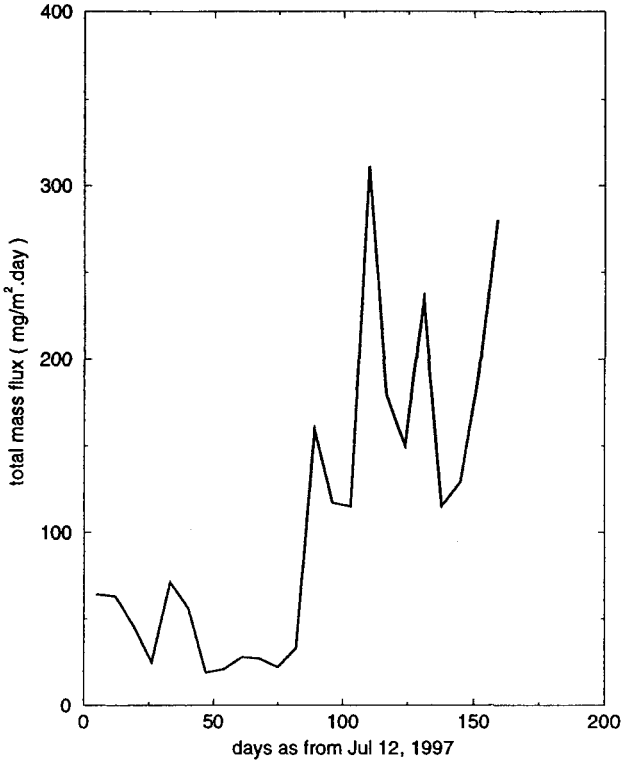

Figure 4.7: Total mass flux of sediments at the ANTARES site as a function of time from July to December 1997.

4.2.3 Transmission properties of the water

The water transparency affects the muon detection efficiency, while the amount of scattered light determines the limit on the angular resolution of the detector. These two parameters therefore influence the detector design and are necessary data for the Monte Carlo simulations from which the detector response is calculated. They must be measured *in situ*, as water samples may be degraded when brought to the surface. Two different experimental setups have been constructed to measure these parameters.

In December 1997, measurements were performed with a 33 m long rigid structure holding a collimated and continuous LED source located at a variable distance from an optical module. For each selected distance D between the source and the detector, the LED luminosity Φ_{LED} was adjusted so as to yield a constant current I_{PMT} on the photomultiplier tube. The set-up was calibrated with a similar experiment done in air. The emitted and detected intensities in water being related by

$$I_{\mathrm{PMT}} \propto \Phi_{\mathrm{LED}}/D^2 \times \exp(-D/\lambda_{\mathrm{att.eff}})$$

this test makes it possible to estimate the effective attenuation length from the dependence of the required LED intensity with the distance (cf. figure 4.8). The agreement of the data with a decrease following the formula given above was excellent and yielded an effective attenuation length of

$$\lambda_{\mathrm{att.eff}} = 41 \pm 1\,(\mathrm{stat.}) \pm 1\,(\mathrm{syst.})\,\mathrm{m} \quad (\mathrm{December\ 1997})$$

This attenuation length results from a combination of absorption and scattering. The experimental set-up was unable to separate these, and the long rail made deployment difficult. The experiment was therefore redesigned so that it used a pulsed source, to facilitate scattering measurements, and a flexible structure to improve ease of deployment.

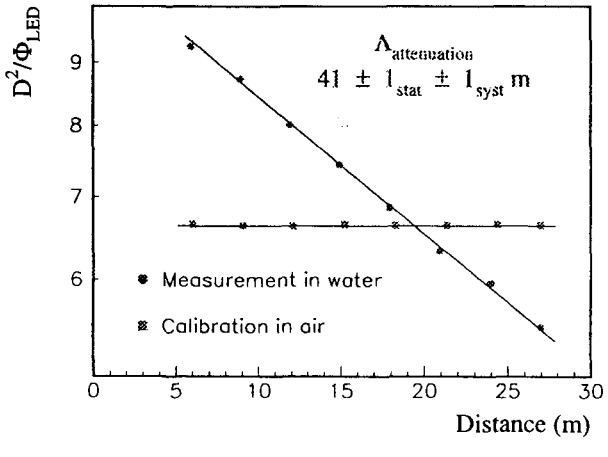

Figure 4.8: Determination of attenuation length. The log of D^2/flux is plotted against D, the distance between the LED and the optical module.

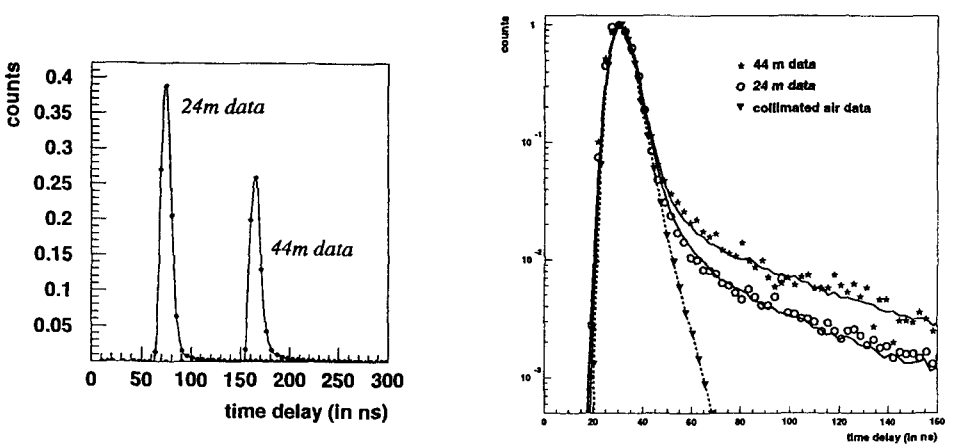

Figure 4.9: (left) Distribution of arrival times of photons for two distances between the detector and the source. The 24 m distribution is normalized to 1, and the 44 m distribution is normalized relative to the first one. (right) Arrival time distributions for 24 m, 44 m, and a calibration in air, with Monte Carlo curves superimposed.

In July 1998 and March 1999, measurements were performed with a set-up consisting of a pulsed isotropic LED source located at a distance of either 24 m or 44 m from a 1″ fast photomultiplier tube. An 8-bit TDC measured the distribution of the arrival times of the photons. The overall time resolution was $\sigma = 4.5$ ns. Because of this, photons in the tail of the distribution have scattered with an angle at least $\sim 35°$ for the 24 m spectrum, and $\sim 25°$ for 45 m. Therefore, the scattering properties of the water are being measured for large scattering angles.

The time distributions recorded exhibit a peak stemming from direct photons, and a tail extending to larger delays due to scattered photons. For the 24 m (44 m) spectrum, 95% (90%) of the photons are collected within 10 ns. Scattering is thus a small effect at the ANTARES site, as illustrated in figure 4.9.

An effective attenuation length could be determined from the ratio of the integrated spectra measured at the two distances, yielding:

$$\lambda_{\mathrm{att,eff}} = \begin{cases} 60.0 \pm 0.4\ (\mathrm{stat.})\ \mathrm{m} & (\text{July 1998}) \\ 52.2 \pm 0.7\ (\mathrm{stat.})\ \mathrm{m} & (\text{March 1999}) \end{cases}$$

A systematic uncertainty of a few metres might affect these estimates due to the fact that the LED luminosity is not monitored and yet assumed to be the same for the time distributions collected at the two distances. These measurements indicate more significant attenuation in March than in July. The difference between these and the December 1997 measurement is also significant, although it is partly accounted for by the use of a collimated source in 1997.

A more detailed analysis can be done by fitting the data with a Monte Carlo distribution obtained by photon tracking. The data are well described using an absorption length in the range 55–65 m, a scattering length at large angles greater than 200 m and a roughly isotropic scattering angle distribution. This is consistent with the effective attenuation length deduced from the ratio of integrated spectra.

4.3 Sea conditions

Suitable sea conditions for periods of up to a few consecutive days are required to perform deployment and recovery operations. These conditions depend both on the nature of the operations and on the characteristics of

the ship. For the single string deployment and recovery operations of June-September 1998 with the *Castor*, a wave height less than 1.5 m and wind speed less than 25 knots (5 on the Beaufort scale) were specified.

A study has been made incorporating data from a number of sources, namely:

- data on wave height collected by an instrumented buoy moored 4 nautical miles south of Porquerolles Island from May 1992 to September 1995, which should be representative of the conditions in the ANTARES site;

- data on the wind speed and direction as recorded by the Porquerolles Island Signal Station analysed for the period from January 1992 to March 1996;

- additional information on sea conditions provided by satellite measurements in the area from 1992 onwards.

Preliminary analysis of these data has been performed by the Meteomer company. Periods of three consecutive days with favourable sea conditions occur less than five times per month from October to April, and more than five times per month from May to September.

4.4 Site survey

The strength and direction of the underwater currents need to be taken into account in the mechanical design of the detector. Figure 4.10 summarises all the measurements of the deep sea current gathered during the test immersions. The maximum current observed, namely 18 cm/s, is accommodated in the mechanical design of the strings.

A visual and bathymetric survey of the sea floor was performed in December 1998, using the *Nautile* submarine. In the area selected as a potential ANTARES site, the sea floor is flat and displays no topographical anomalies such as steps or rocks, as can be seen in figure 4.11. During the same series of dives, core samples from the sea floor were collected. They consist of solid mud which is a satisfactory substrate to support the detector.

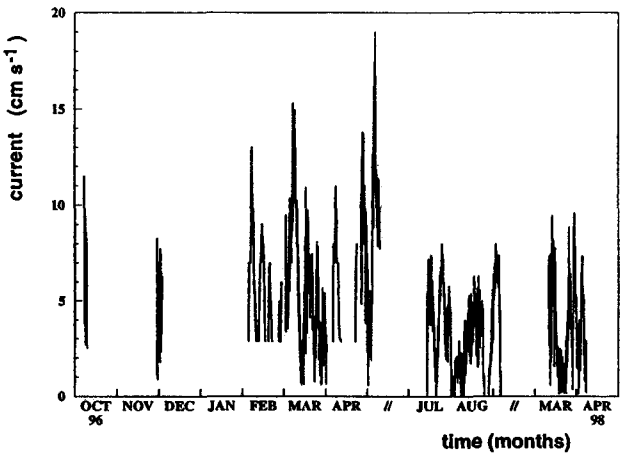

Figure 4.10: Summary of the survey of deep sea currents.

4.5 Prototype string

To gain realistic experience of the issues involved in the deployment, operation and recovery of a full-scale detector, a full-size prototype of an ANTARES detector string has been constructed. It is equipped with a positioning system, slow control network, power distribution, and eight optical modules with their associated readout electronics. Once deployed, the string is foreseen to be linked to a shore station by an electro-optical cable supplying the power to the string as well as enabling the control and readout connection. The string is adequate for a detailed study of the optical background and a measurement of the down-going muon flux.

4.5.1 Mechanical structure

The prototype string is 350 m high (figure 4.12), anchored on the sea floor and vertically supported by a buoy. It is composed of two vertical cables spaced 2.3 m apart, supporting both ends of sixteen Optical Module Frames (OMFs). The OMFs are placed every 15 m from a height of 95 m up to 320 m from the sea floor and are constructed from fibre glass to avoid corrosion. Horizontal spacers keep the vertical support cables below the lowest OMF; a spacer is also situated at the middle of every 15 m segment separating the OMFs.

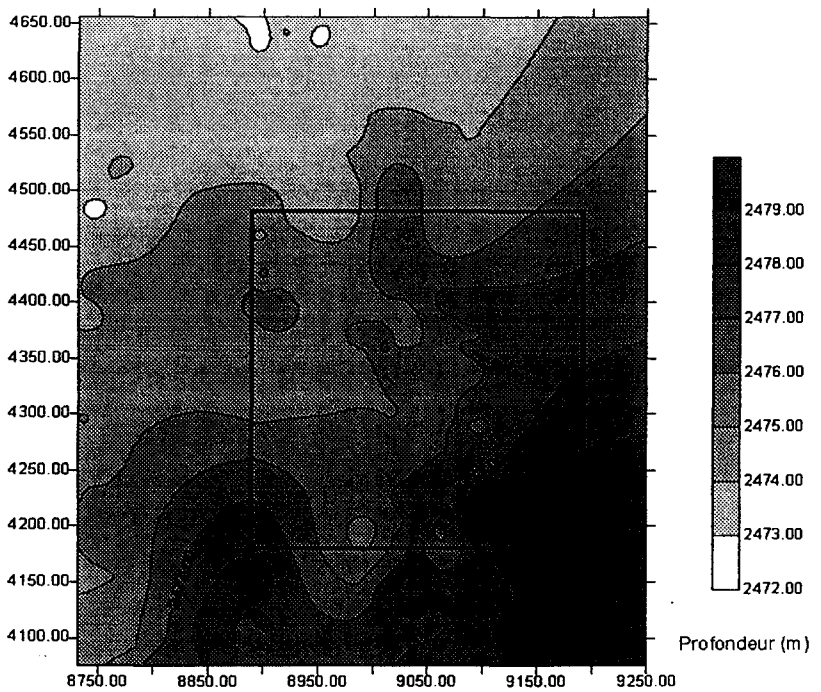

Figure 4.11: Site survey map

Each OMF supports a pair of Optical Modules, separated by 1.6 m from axis to axis, while the central part houses a container for electronics made of corrosion-resistant titanium alloy.

4.5.2 Slow control system

A slow control network is linked to the shore station through an electro-optical cable and employs an architecture whereby each electronics container has a point-to-point connection with the slow control data acquisition system. It permits the control of the power distribution electronics, optical module motherboard, analogue readout electronics and the acoustic positioning system. It also handles the readout and transmission of sensor data, such as the satellites, the acoustic system and the electronic card temperatures or status.

This DAQ system is located in the main electronics container at the

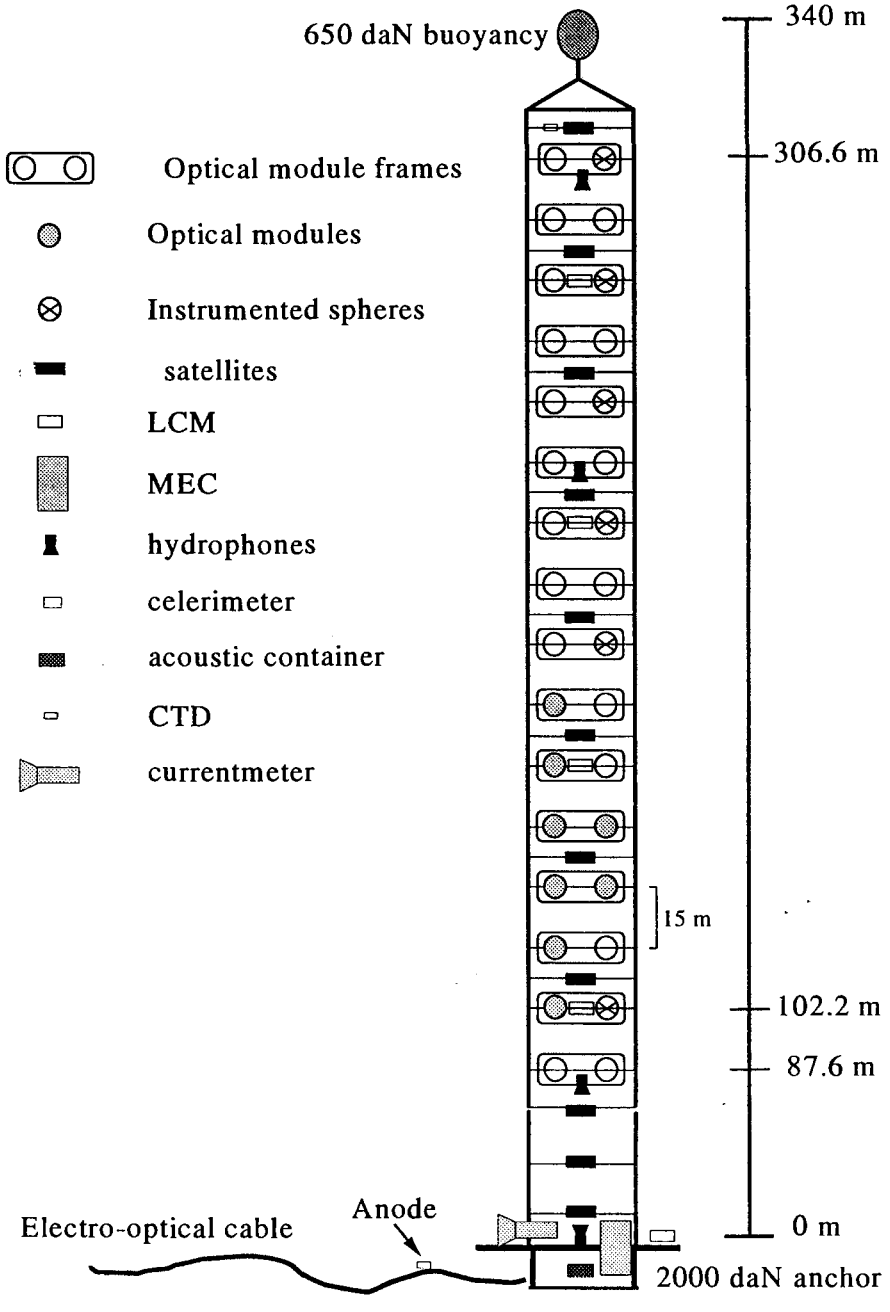

Figure 4.12: Schematic view of the prototype string.

bottom of the string. The main fibre-optic data link connects this system to the shore station, which receives the slow-control data and provides a user interface for the slow-control system.

4.5.3 Positioning

A string does not provide rigid support for the optical modules. Two independent systems have been incorporated in the prototype string to provide a precise knowledge of the relative position of each OM at any time. The first system is based on a set of tiltmeters and compasses which measure local tilt angles and orientations on the string. The reconstruction of the line shape, as distorted by the water current flow, is obtained from a fit of measurements taken at different points along the line. A successful test of this system was performed during a deployment of the prototype string which was equipped with several sensors with a precision of 0.05° in tilt and of 0.3° in direction. Figure 4.13 presents a view of the reconstructed line, the segments indicating the sensor positions and directions with respect to North. A maximum error of $\sim$ 1 m on the reconstructed shape is estimated.

The second system, based on acoustic triangulation, is more precise but requires more complex and expensive electronics. In this system, rangemeters placed on the string send an acoustic signal to a minimum of three transponders fixed to the sea bed. Each transponder replies with its characteristic frequency. A global fit of the measured acoustic paths gives the precise three-dimensional position of the rangemeters, provided that the positions of the transponders and the sound velocity in water are known. The prototype string is equipped with four rangemeters (a hydrophone with its electronics container) communicating with four external autonomous transponders placed on a fixed structure on the sea floor about 200 m away from the string. The measurement of the communication time between one fixed rangemeter and one fixed transponder demonstrates a reproducibility of $\sim$ 1 cm in the acoustic path length (figure 4.14).

In order to exploit such a system fully, a precise knowledge of the sound velocity in water along the acoustic path is required. This depends strongly on water temperature and also on salinity and depth. The prototype string is thus equipped with sound velocimeters, which measure the local sound velocity with a precision of 5 cm s^{-1}, and with Conductivity Temperature Depth devices (CTDs) to observe the variations of temperature and salinity.

The systems are complementary: a few points of the line can be measured

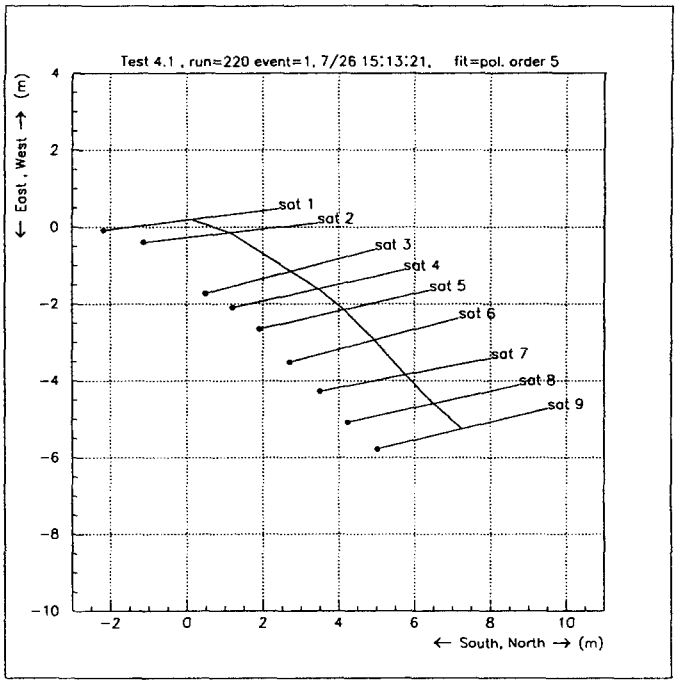

Figure 4.13: Top view of the reconstructed shape of the prototype string during deployment, sensors are labelled *sat 1* to *sat 9*

acoustically and other points are obtained by line shape fitting. The tests already performed confirm that the desired precision on relative OM positioning can be achieved.

4.5.4 String deployment

The prototype string was deployed, operated and retrieved several times in Summer 1998, first at 400 m depth and then at 2300 m. This string was powered by batteries housed in a container at the bottom of the string. The deployment procedure used was different from that used for the mooring lines discussed earlier. In this case, a step-by-step procedure involving two winches on the boat deck was implemented whereby the anchor was immersed first, the string being held securely at 2 points, then each OMF was paid out storey-by-storey. Recovery was performed in a similar way. Deployment and recovery at 2300 m took 18 hours in total. This method allowed the equipment to be deployed in a safe and controlled manner. The exercise also

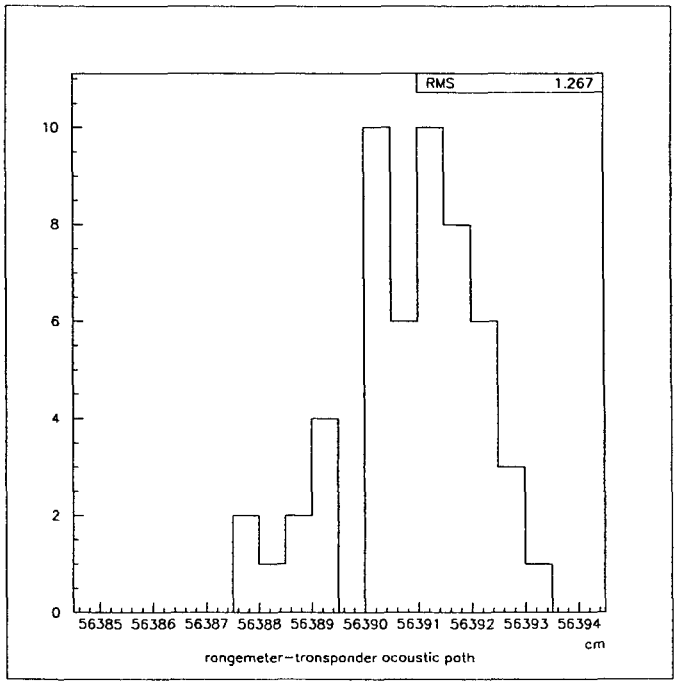

Figure 4.14: Distribution of the acoustic path measurement between a fixed rangemeter and a fixed transponder.

permitted the handling procedures for the electro-optical cable termination attached to the string anchor to be verified. The tiltmeter and compass data were recorded so that the detector string behaviour could be studied during the deployment phase. The fully equipped version of the prototype string will be ready for immersion during Summer 1999.

Successful deployment of the 0.1 km^2 array will require strings to be located in well-defined positions with 80 m spacing or less. This was investigated in a multi-string deployment test using the dynamical positioning ship *Provence* and 400 m test strings instrumented with acoustic beacons.

String positioning precision was investigated by aiming to deploy a second test string 50 m away from the one which had been deployed earlier. Relative positions were measured with the aid of three external acoustic beacons.

The second string was deployed using a winch, with the ship located at the target position. Deployment was halted with the string 200 m above the sea floor, the relative position measured, and the ship moved to adjust as

necessary. Using this technique it proved possible to locate the second string to within 10 m of the nominal position.

4.5.5 Deep sea connection and line recovery

In the full-scale detector, each string will be connected to a common point, known as the junction box. A connection scheme from the junction box to a prototype string anchor was tested during a ten-day sea operation at the ANTARES site, using the *Nautile* submarine and its support vessel the *Nadir* from IFREMER.

A reel of cable equipped with deep sea connectors on both ends was immersed first. Then the *Nautile* uncoiled the cable by pulling it and plugged the connector of the cable to its counterpart on the anchor. The connection procedure was successfully performed twice, using a free-flight technique which requires only one of the submarine's arms. This offers the possibility of using IFREMER's second manned submarine, the *Cyana*, which is equipped with only one arm. The advantage of this is that this submarine is more freely available than the *Nautile*.

Figure 4.15 shows a diagram of the *Nautile* approaching the anchor, holding the connector and the cable, before plugging it at the end of the arm which can be seen in an upright position at the bottom of the string. Once the connection is made, the *Nautile* pushes the arm down and plugs it into a fork linked to the anchoring weight. To retrieve the string, acoustic releases are activated from the surface which disconnect the string from the anchoring weight. The buoyancy of the string pulls on the connector which is held back by the fork and is thus unplugged. This system avoids the need for a submarine for string retrieval.

The speed of ascent of the string during its trip to the surface is around 1 m s^{-1}. The distribution of weights and buoyancies along the string have to be carefully studied in order to control the relative speed of each storey so that the string does not become entangled when it surfaces.

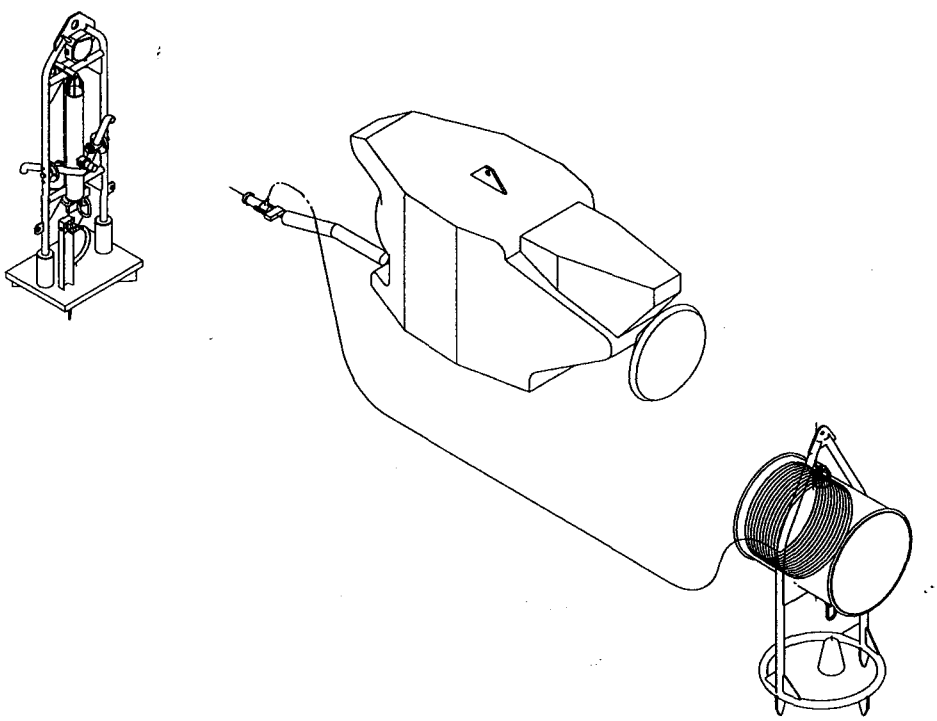

Figure 4.15: Deep sea connection test using the *Nautile* submarine.

Chapter 5

Detector design

The detector design described in this chapter is constrained by the following factors:

- the environmental conditions at the site, which influence the spacing of optical modules, the mechanical structure of detector strings, and the expected background rates;
- the practical experience gained from the design and deployment of the protoype string;
- the need to optimise the physics performance of the detector;
- the requirement for a high level of reliability.

The first two issues were discussed in the preceding chapter, and the physics performance and its optimisation are the subject of chapter 6. A key issue throughout the detector design is the question of reliability. Repair and maintenance of offshore detector elements will involve high costs and probably long down times, and must be minimised. For this reason, the design of each of the detector components discussed in the subsequent sections will follow a strategy intended to enhance reliability: reduction of the number of active components, limitation of power consumption, and avoidance of single-point failure modes.

This chapter outlines the specifications satisfying these constraints. The design may evolve further as technical details are refined and additional physics simulations are performed.

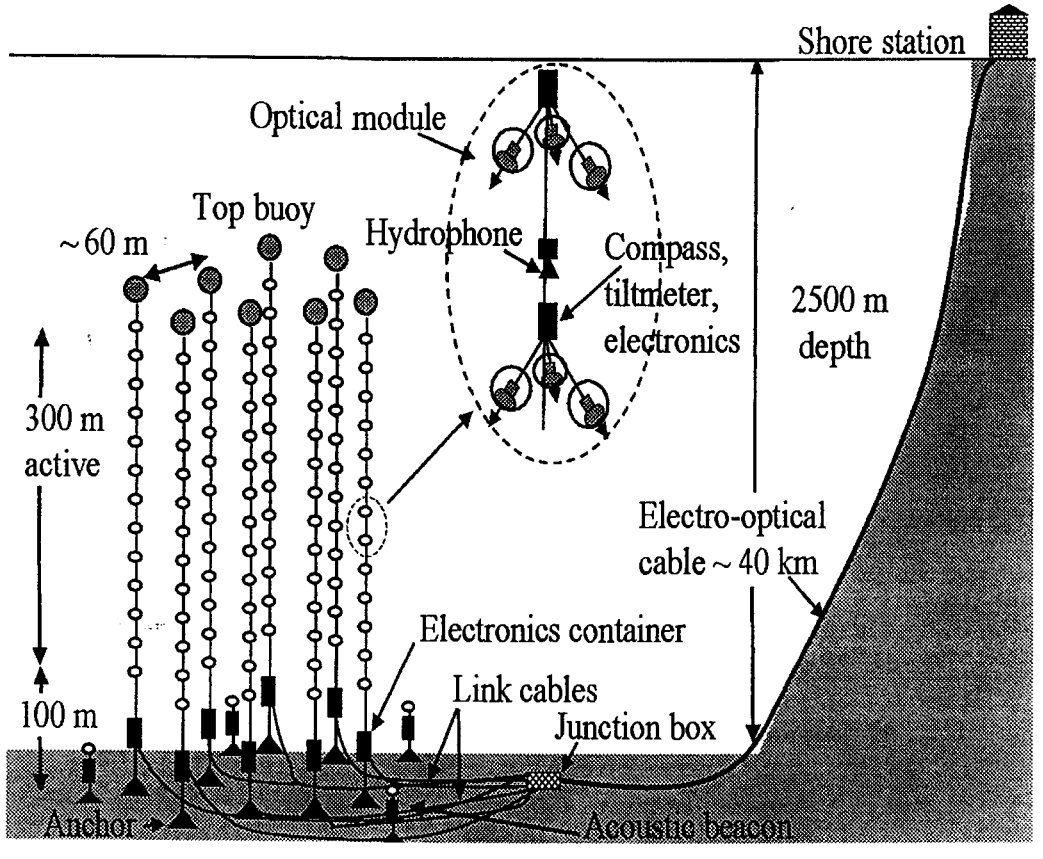

Figure 5.1: Schematic of part of the detector array; the magnified view shows two storeys and a hydrophone.

5.1 Overview

The detector consists of an array of approximately 1000 photomultiplier tubes in 13 vertical strings, spread over an area of about 0.1 km^2 and with an active height of about 0.3 km. Figure 5.1 shows a schematic view of part of the detector array indicating the principal components of the detector.

The basic unit of the detector is the optical module, consisting of a photomultiplier tube, various sensors, and the associated electronics, housed in a pressure-resistant glass sphere. The electronics includes a custom-built digital electronic circuit which captures and stores waveforms, pulse

heights and timing information, as well as the HV power supply for the photomultiplier tubes and the network nodes for data transmission and slow control.

The optical modules are grouped together in 'storeys' of three modules and interconnected via an electro-mechanical cable. In the present design the detector has 13 strings, each of which has a total height of about 400 m. Of the 13 strings, four consist of 41 storeys spaced vertically by 8 m and nine have 21 storeys spaced vertically by 16 m. The strings are arranged in a randomized spiral (see figure 6.7) with a minimum horizontal spacing fixed at some value between 60 m and 80 m. The smaller spacing gives a higher detection efficiency for muon energies up to 50 TeV but could be more difficult to deploy.

The optical modules in a storey are arranged with the axis of the photomultiplier tubes 45° below the horizontal. The present plan is to use 10-inch Hamamatsu photomultiplier tubes, but other, possibly larger, tubes are under development by various manufacturers. The angular acceptance of the optical modules is broad, falling to half maximum at $\pm 70°$ from the axis (see below). This means that the proposed arrangement of OMs detects light in the lower hemisphere with high efficiency, and has some acceptance for muon directions above the horizontal. In the lower hemisphere there is an overlap in angular acceptance between modules, permitting an event trigger based on coincidences from this overlap.

The relative positions of all optical modules in the detector are given in real time by a positioning system identical to that described for the prototype string in section 4.5.3.

Each string is instrumented with several electronics containers. At every storey, there is a local control module (LCM), and at the base of each string there is a string control module (SCM). Special containers house acoustics and calibration equipment. Each of these containers constitutes a node of the data transmission network, receiving and transmitting data and slow-control commands. The functions which they support include reading sensors, adjusting slow-control parameters, the trigger, and the distribution of power, master clock and reset signals to the front-end electronics.

The individual SCMs are linked to a common junction box by electro-optical cables which are connected using a manned submarine. A standard deep sea telecommunication cable links the junction box with a shore station where the data are filtered and recorded.

The trigger logic in the sea is planned to be as simple and flexible as

possible. The first-level trigger requires a coincidence between any two OMs in a single storey. The second-level trigger is based on combinations of first-level triggers. Following a second-level trigger the full detector will be read out. A more refined third-level trigger, imposing tighter time coincidences over larger numbers of optical modules, will be made in a farm of processors on shore. The readout rate is expected to be several kHz, and the corresponding data recording rate less than 100 events per second.

The following sections of this chapter describe the various components of the detector in more detail.

5.2 Detector string

The design chosen for the detector string is similar to that used for the prototype string described earlier in chapter 4, a string maintained vertically by its own buoyancy and anchored on the bottom of the sea. Between the buoy and the anchor, the active detector part of the string comprises a series of elementary detector segments. These segments are standardised and so can be mass-produced, and if necessary interchanged.

In all cases, the design of the string components meets basic specifications such as corrosion resistance, required because of the prolonged immersion in salt water, resistance to high pressure and water-tightness. Similarly, in certain cases, the colour and surface properties of detector elements need to be selected so as to minimize light reflection. All detector components must remain functional for a minimum lifetime of 10 years.

The principal elements of each string are illustrated in figure 5.2 and discussed further here.

The bottom string socket (BSS) anchors the string to the sea bed, facilitates the electrical connection of the string to the network and permits the release and subsequent retrieval of the string. To allow precise and simple string installation its construction has been optimised for handling on the deployment ship, resistance to shock, stability during descent. The BSS is instrumented for acoustic positioning. Connection of the string to the network is performed by a submarine and is described in section 4.5.5.

The electro-mechanical cable (EMC) provides mechanical support for the string as well as enabling the electrical interconnection of the detector string elements. It must be capable of supporting tensile, torsion and bending stresses in order to maintain the string's stability. Its construction must be

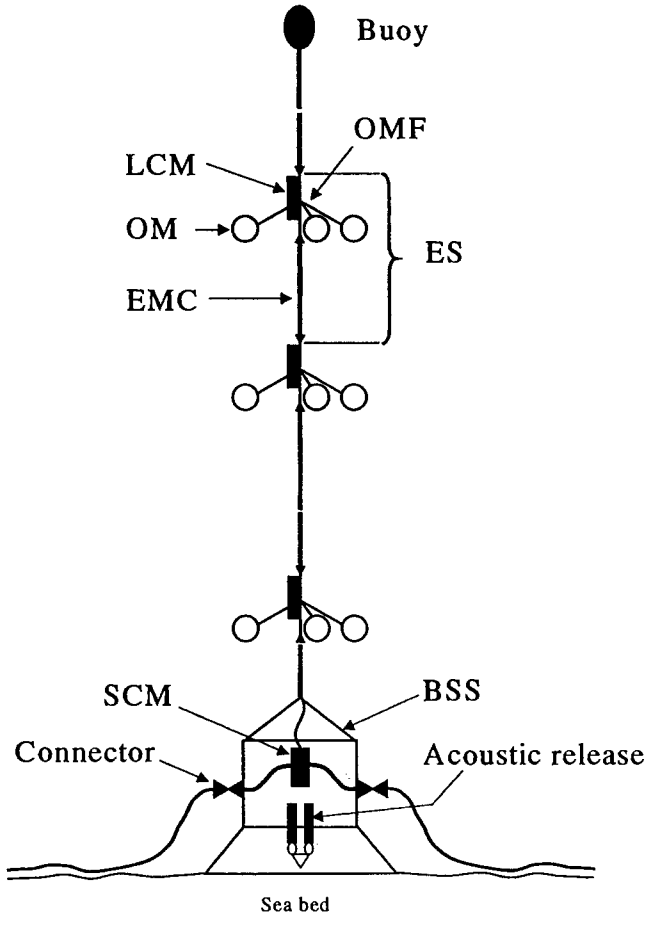

Figure 5.2: Sketch of the detector string, abbreviations are defined in the text.

suitably flexible to allow the integration of the various configurations, as well as supporting the service, storage, handling and immersion and recuperation phases. Electrical cables and optical fibres run through the EMC. They enable power distribution and the transmission of signals between two consecutive electronic containers (LCM or SCM).

Each elementary segment (ES) consists of three optical modules, one local control module and one optical module frame. The OMF supports the various elements placed within it, namely the optical modules, the LCM container and possibly a hydrophone for acoustic positioning. The OMF design must be sufficiently flexible to accept certain changes in the number and positioning of the optical modules. Major traction forces that work on the substructure during deployment and recovery must in no way be transmitted to those string elements supported by the frame.

The top of the string consists of a buoy. Its dimensions and geometry are optimised to minimise hydrodynamic effects such as dragging and vibration whilst maintaining a suitable tension in the string. In addition, the buoyancy should be sufficient to ensure a controlled resurfacing of the string during retrieval.

5.3 Optical module

A schematic view of the ANTARES optical module is shown in figure 5.3. Mechanical and optical aspects of the OMs are reviewed in this section, as well as the performance of the various photomultiplier tubes which have been evaluated.

5.3.1 Benthos sphere

The photomultiplier tube and its associated electronics are housed in a 43 cm diameter, 15 mm thick, Benthos sphere, which can withstand pressures of up to 700 bars. The sphere is made of two halves, one of which is painted black on its inner surface so as to give the OM some minimal directionality with respect to Cherenkov light detection without degrading its acceptance. The two halves of the sphere have machined edges which form a seal when subjected to an external over-pressure. Attenuation of light at $\lambda = 450$ nm due to the sphere was measured to be less than 2% (see figure 5.4).

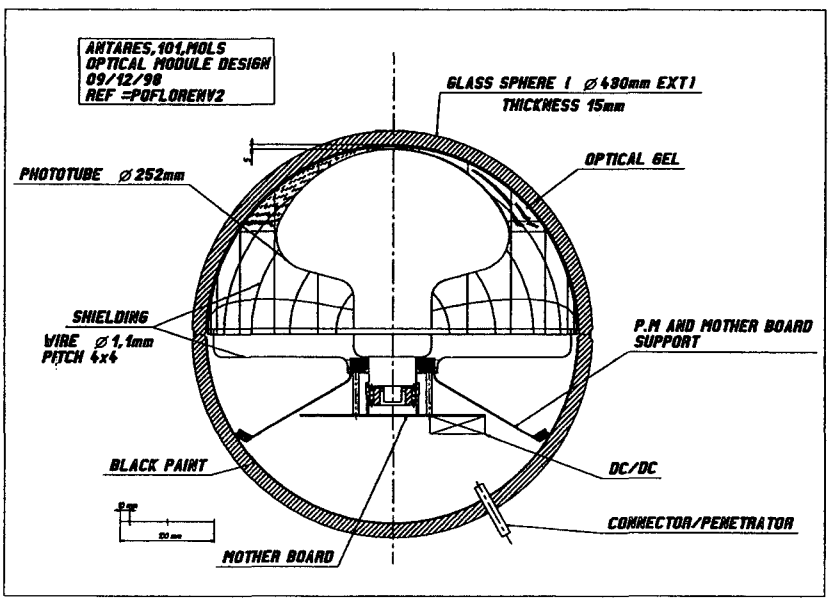

Figure 5.3: Cross section of the optical module.

5.3.2 Optical contact and magnetic shielding

Silicone gel ensures both optical coupling and mechanical support of the PMT. The refractive index of the gel ($n_{gel} = 1.40$) does not exactly match that of the sphere itself ($n_{glass} = 1.48$) but is higher than the refractive index of water ($n_{water} = 1.35$) and so the amount of light reflected out of the OM is minimized. The silicone gel covers the entire photocathode area; its attenuation length is given as a function of wavelength in figure 5.4 [57].

The Earth's magnetic field significantly degrades the collection efficiency of phototubes by bending the trajectories of electrons, mainly between the photocathode and the first dynode. A cage made of 1.1 mm thick high-permittivity alloy wire is used to shield the PMT and to minimise the dependence of the OM response with respect to its angle with the magnetic North. The mesh size of the cage (6.8 cm) was optimized to reduce the non-uniformity of the PMT angular response to less than 5% while minimizing the fraction of light lost due to the shadow on the photocathode [58].

5.3.3 Photomultiplier tube characterisation

During the last three years several test benches have been set up to measure and compare the principal features of different PMTs and to provide detailed characteristics of the OM response. These include several 'dark boxes', in which the PMTs are exposed to uniform illumination coming from red, green or blue LEDs or very fast solid-state lasers. This allows the systematic and precise measurement of a large number of PMT characteristics [60]. Several PMTs of different diameters have been studied, and their performances are summarised here in terms of a small number of critical parameters. This discussion only considers a fraction of the total number of parameters which have actually been measured (see [59, 60, 61]).

The effective photocathode area (A_{eff}^{PC}) is defined as the detection area of the photocathode weighted by the collection efficiency. It was measured by scanning the entire photocathode surface with a collimated blue LED.

Electromagnetic interference in the optical module induces noise at the PMT anode. It is expected that this will not exceed 5 mV (rms). This noise governs the gain at which the PMT is operated. A factor of 10 between the average pulse height for a single photo electron (SPE) and the noise is sufficient to ensure efficient discrimination of the signal. This corresponds to an effective working gain of the order of 5×10^7. In view of PMT ageing and possible variations in specifications a maximum gain of at least 10^8 is required.

The Peak to Valley ratio is computed from the observed charge spectrum of single photoelectrons with the high voltage adjusted to give 50 mV amplitude for SPE. The Peak to Valley ratio is required to be greater than 2.

Due to imperfections in the electron optics and the finite size of the photocathode, the SPE transit time between the photocathode and the first dynode has a measurable width, usually referred to as the transit time spread (TTS). This defines the timing resolution of the PMT, which is required to be comparable to that from the overall positional accuracy and the timing precision in the readout electronics, i.e. 1.3 ns rms or 3 ns FWHM. The measurement of the TTS is performed over the whole photocathode area with the PMT operating at a gain of 5×10^7.

Four different PMTs are compared in table 5.1. The maximum quantum efficiency, the linearity and the dark count rate have also been determined.

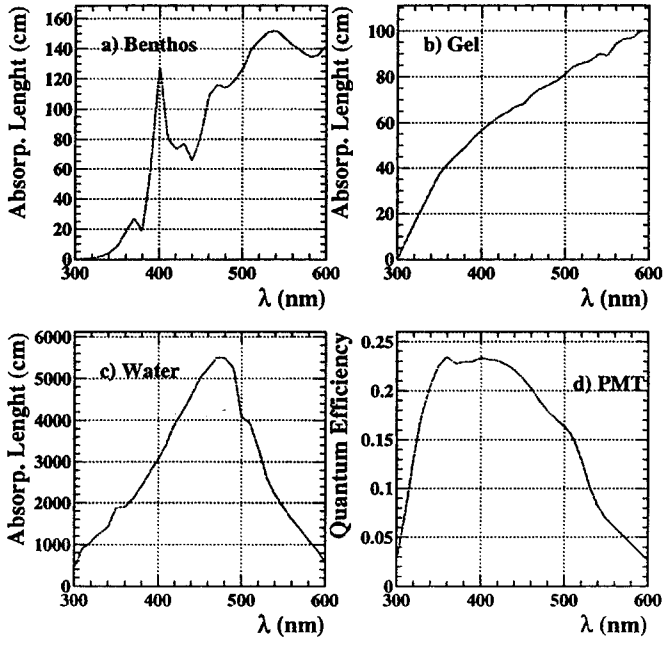

Figure 5.4: Attenuation length of (a) the Benthos sphere, (b) silicone gel and (c) sea water; (d) quantum efficiency for the Hamamatsu photomultiplier tubes.

5.3.4 Optical module response

To reproduce the experimental conditions, it is necessary to investigate the response of an optical module to the Cherenkov light produced by muons travelling through water. This has been studied by placing an OM in a 1.5 m high, 1.4 m diameter, light-tight cylindrical steel tank filled with constantly recycled fresh water [61]. Nearly-vertical atmospheric muons are tracked in a four plane hodoscope, two planes above the tank, two below. Between the tank and the two lower planes a lead shield ensures $E_\mu > 0.6$ GeV. Muons traverse the tank and produce Cherenkov light which illuminates the optical module. The light yield for muons of this energy is more than 90% of the value for a single relativistic track. The optical module is able to rotate, so that its response can be measured at different angles, θ_{OM}, between the incident muon and the PMT axis.

Manufacturer	Hamamatsu		ETL	
Phototube diameter	8″	10″	8″	11″
A_{eff}^{PC} (cm^2)	280	440	240	620
Maximum gain	10^9	10^9	10^8	5×10^7
Peak to valley ratio	2-3	3-3.5	< 2	2
TTS (FWHM) (ns)	2.5	3.5	2.5	3.0

Table 5.1: Comparison of relevant properties of large-photocathode phototubes tested to date.

Figure 5.5 presents results from this setup using an optical module equipped with a 10″ tube. The angular region where the OM sees more than half the maximum amplitude is of the order of $\pm 70°$.

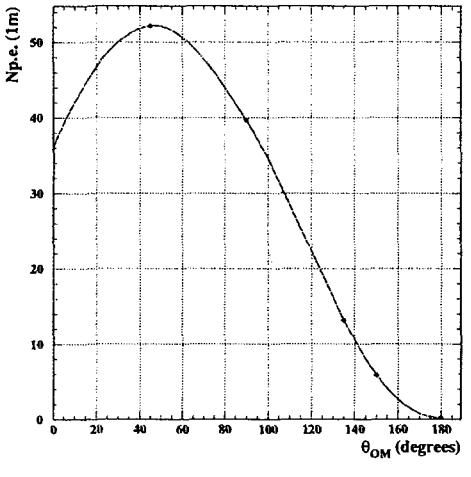

Figure 5.5: Number of photo-electrons detected by the optical module as a function of its zenith angle θ_{OM}, for nearly vertical muons normalised at 1 m distance.

5.4 Offshore electronics

The distance between the detector and land precludes a point-to-point connection between each optical module and the shore station. Instead, an electro-optical cable from the shore station supplies electrical power to the detector array and permits data to flow in both directions. The electro-optical cable ends at the junction box to which the strings are connected. A star-topology network architecture is used, running from the string control module to the optical modules via the local control modules. A digital scheme has been developed for the necessary data multiplexing.

This network is used to distribute power, collect data, broadcast slow control commands and master clock signals, and form the trigger. This section describes the implementation of the above scheme.

5.4.1 Digital front end

The OM electronics must fit in the limited space available in the OM, consume little power, be reliable and long-lived (average lifetime > 10 yr), be inexpensive.

An Application Specific Integrated Circuit (ASIC) meets these requirements and can be tailored to our needs. The ASIC developed for the digital front end is called the Analogue Ring Sampler (ARS), similar in design to the Analogue Transient Waveform Recorder [62]. The chip samples the photomultiplier tube signal continuously at a tunable frequency between 300 and 1000 MHz and holds the analogue information on 128 switched capacitors when a low-level threshold is crossed. The information is then digitized by an external 8-bit ADC. Figure 5.6 shows the resulting histogram for an effective sampling frequency of 1000 MHz.

A 20 MHz reference clock is sampled on one channel, giving a relative timing of the signals to better than 1 ns. A time stamp is obtained for each event by counting the reference clock cycles. A reset command sent through the clock stream is used to restart all the counters of the array synchronously.

Since 99% of the pulses are single photo-electrons, another ASIC, dedicated to the treatment of single photo-electron pulses, has been developed in order to reduce the dead time and the data flow. The first part of the ASIC performs pulse shape discrimination (PSD). It identifies three types of pulses requiring analysis of the full wave form:

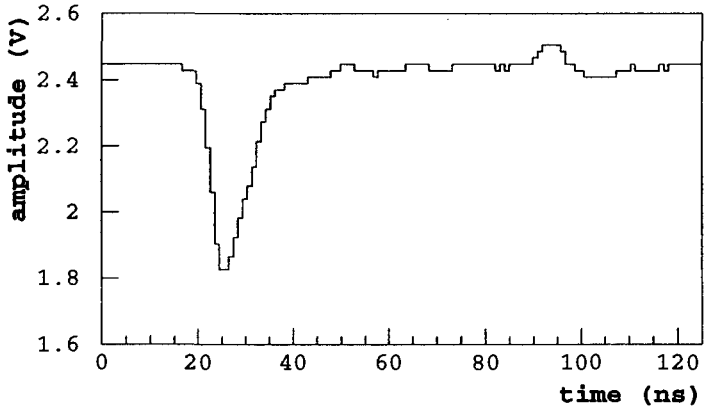

Figure 5.6: Charge measured in the 128 switched capacitors of the ARS memory after the capture of an analogue signal from a photomultiplier tube. The reflection of the signal comes from an impedance mismatch on the test board.

- large pulses, with pulse heights that cross a threshold corresponding to several photo-electrons;
- wide pulses, with time over a low threshold longer than about 15 ns;
- two pulses separated by less than 50 ns.

If none of these conditions is met, only the pulse charge and time of arrival are measured, this information, along with the OM address, is transmitted to shore in 64 data bits. The large pulse threshold, the time over threshold, and the time window for multiple pulses are adjustable. The remaining 1% of the pulses satisfy one of the three conditions above and so the pulse shape is transferred for offline analysis, approximately 2000 data bits are required to encode this type of event (waveform event).

A new version of the ARS is currently under development. It integrates all these functions on the same chip, together with the ADCs, the DACs and the slow-control interface (figure 5.7). A pipeline memory is implemented to store the single photo-electron information long enough to match the level 2 trigger propagation and formation time, which is around 10 μs for a 0.1 km^2

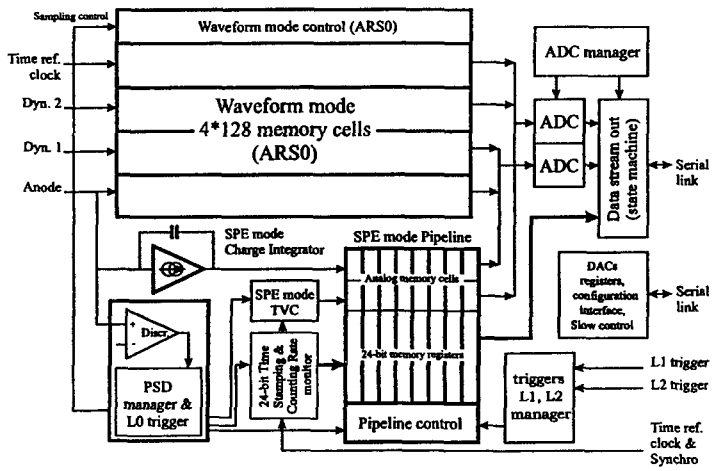

Figure 5.7: ARS1 block diagram.

detector. It will be possible to use up to four memories per optical module, in a token ring. This will permit the chip to be used with photomultiplier tubes bigger than 10 inches in diameter, for which the counting rate may exceed 60 kHz, and for a km-scale detector, where the trigger formation and propagation time may reach 30 μs.

5.4.2 Trigger logic and rates

A level 0 trigger occurs when the output of a photomultiplier tube crosses a threshold corresponding to 30 % of a single photo-electron amplitude. In order to deal with the high counting rate in the sea (see section 4.2.1), a level 1 trigger is built out of a tight time coincidence between two level 0 triggers from the same storey. A level 2 trigger can be formed by requiring multiple level 1 triggers in a coincidence gate whose width is of the order of that needed for a track to pass through the entire detector. The level 2 trigger condition could be at least two level 1 triggers on the same string (referred to as the 'string trigger') or at least three level 1 triggers anywhere in the detector (referred to as the 'array trigger'). When either the string trigger or the array trigger conditions is satisfied, a readout request is sent to the entire array. The readout request is received in each OM, which starts the digitization of all the information within the maximum allowed time of flight.

Internal delays specific to each OM compensate for the trigger formation and readout request propagation times. When a level 1 trigger occurs in a storey, the two OMs involved are read out, even if they do not participate in the subsequent level 2 trigger.

The level 1 trigger logic will be installed in each LCM. The level 2 trigger logic must be linked to all the LCMs which may participate in the trigger: therefore the array trigger will be installed in the junction box, while the string trigger will be installed at the bottom of each string, and then sent to the junction box, from which the readout request will originate.

Trigger rates due to random coincidences from background counting rates have been estimated assuming a level 0 trigger rate of 60 kHz. The level 1 trigger requires a coincidence between two of the three optical modules on any storey with a pulse width of 20 ns, yielding a rate about 500 Hz per storey.

Level 2 trigger rates are calculated assuming four dense strings of 41 storeys with 8 m vertical spacing, and nine sparse strings of 21 storeys with 16 m spacing. The gate width for string triggers is 1.5 μs, the time for a particle to travel the length of the string. For array triggers, which involve multiple strings, a coincidence width of 2 μs is used. A simple string trigger requiring two level 1 triggers on the same string leads to a level 2 trigger rate of about 3 kHz. A similar array trigger requiring three level 1 triggers within the 353 storeys of the full detector adds 6 kHz, yielding a total level 2 trigger rate of about 10 kHz.

More restrictive level 2 triggers can be obtained by combining signals from separate sectors on a single string to yield 'proximity' triggers, favouring nearby hits on the same string. The time for light to traverse two sectors is 400 ns. Requiring two level 1 triggers within two adjacent sectors leads to a total rate of 300 Hz, down a factor 10 from the simple string trigger described above.

Even more restrictive level 2 triggers can be defined if necessary. The easiest way to reduce the trigger rate is to increase the number of level 1 triggers required within the level 2 coincidence gate. For the simple string triggers, requiring three level 1 triggers would reduce their contribution to the level 2 trigger to about 30 Hz, a reduction of a factor 100. For the array triggers, requiring four level 1 triggers in coincidence would reduce the level 2 rate to about 600 Hz, a reduction of a factor 10.

During a bioluminescence burst, level 1 triggers from affected storeys provide no discrimination against noise, because all the OMs in the storey

see the burst. These storeys are removed from the trigger logic in real time, but the OMs are still read out, as the timing resolution of the detector is sufficiently precise to allow real hits to be recovered from the noise when tracks are reconstructed.

5.4.3 Data flow rate

The volume of data transmitted to shore depends on the trigger rate, the OM background and the proportion of waveform events. The following calculation has been performed for a total trigger rate of 10 kHz with a 2 μs time window, so that 2% of the overall background activity is read out and sent to shore. The noise rate from each OM is assumed to be 60 kHz for 95% of the time (quiescent phase) and 300 kHz for the remaining 5% (bioluminescence activity). It is also assumed that the level 1 trigger is disabled for modules undergoing bioluminescence activity.

The three classes of waveform events, namely large pulses, wide pulses and events where two pulses occur within 50 ns are discussed in section 5.4.1. Large or wide pulses originate from decays in or near the OM and amount to a few hundred Hz, while closely spaced pulses can result either from pre- or after-pulsing or from accidental coincidences. At 60 kHz, the three contributions are of approximately equal importance and give about 1 kHz of waveform events, while at 300 kHz, accidental coincidences dominate, yielding about 10 kHz of waveforms.

Given these figures, the data flow rate from the level 2 triggers is 300 Mb/s. Reading out the OMs involved in level 1 triggers adds a further 100 Mb/s to give a total data flow rate of about 400 Mb/s.

5.4.4 Data handling and transmission to the shore

A number of electronic functions must be developed in order to handle the digital data coming from the optical modules and transmit it to shore. Functions are required at each storey on the string (LCM), at the base of the string (SCM), and in the junction box connected to the shore by the electro-optical cable. The specific functions are:

- Organizing data coming from the optical modules and transferring them to the SCM.

- Processing the level 1 trigger at the LCM and the level 2 trigger at the SCM and at the junction box.
- Slow control and monitoring hardware.
- Clock distribution from the shore to the LCM containers and on to the optical modules, in order to time stamp all digitized physical events.
- Handling of the acoustic positioning electronics for each string, distributed over selected storeys throughout the length of the string, performed at the LCM level.
- Acquisition of mechanical positioning information from tilt-meters and compasses incorporated in the LCMs.
- Transmission of data and slow-control commands from the shore to the SCMs via the junction box.

Experience with the prototype string has led to the adoption of the following techniques:

- Fibre-optics along and between strings, providing reliable, compact and high bandwidth links
- Penetrators as opposed to connectors at the level of each LCM: this permits the use of optical fibres, allows connections to be made inside the container, and increases the number of communications channels which can be integrated into a single electro-mechanical cable.

5.4.5 Electro-optical cable and junction box

Existing electro-optical cables designed for submarine telecommunications applications fulfill the power and data handling requirements summarised above. They incorporate a copper coaxial conductor for power transmission and 16 to 24 optical fibres for digital signals.

The junction box contains power converters in an oil bath to provide a standard 400 V DC voltage, the trigger electronics and the electro-optical interface for the data, slow control and clock transmission.

The cable and junction box are a potential single point failure of the detector. It is therefore foreseen to have two cables and two junction boxes, each capable of handling the full requirements of the detector.

Electro-optical cables link the junction box to each SCM. since optical fibres are necessary for the data transmission and the clock distribution. In order to use standard undersea electrical connectors, it is foreseen to convert all optical signals to electrical ones near the connectors.

5.5 Slow control and commands

The system of slow control is intended for the monitoring of variables which change relatively slowly, and also serves to control various aspects of detector operation. PMT voltage, temperature and power-supply voltages are read from the optical modules. Dedicated instruments provide information on string attitude and orientation, water current velocity, acoustic positioning information, and other control data. Parameters to be adjusted during detector operation include the PMT voltage, thresholds involved in pulse detection and triggering, and various calibration systems. The slow control system thus gives a user at the shore station all the information needed to monitor and control the detector, as well as providing the calibration information necessary to reconstruct events.

Slow-control data acquisition and execution of slow-control commands are carried out by the processor on the motherboard of the relevant electronics container (OM, LCM, SCM, or specialized instrumentation container).

5.6 Calibration and positioning

The pointing accuracy of the detector is determined largely by the overall timing accuracy of each event. This is a quadratic sum of terms due to

- the precision with which the spatial positioning and orientation of the optical modules is known (σ_{geom});
- the accuracy with which the arrival time of photons at the optical modules is measured (σ_{pmt});
- the precision with which local timing of individual optical module signals can be synchronised with respect to each other (σ_{align})

$$\sigma_t^2 = \sigma_{pmt}^2 + \sigma_{geom}^2 + \sigma_{align}^2$$

Furthermore, *in situ* calibration of the optical module efficiency as a function of time is necessary in order to measure and correct changes in the response due to factors such as optical fouling. These issues are now discussed in detail.

5.6.1 Positioning

The reconstruction of the muon trajectory is based on the differences of the arrival times of the photons between optical modules. As such, it is sensitive to the distances between the optical modules. In order to avoid degrading the reconstruction, it is necessary to monitor the position of each optical module with a precision of 10 cm (light travels 22 cm per ns in water). The reconstruction of the muon trajectory and the determination of its energy also require knowledge of the optical module orientation with a precision of a few degrees. The precise absolute positioning of the whole detector has to be guaranteed in order to point to individual sources.

To attain a suitable precision on the overall positioning accuracy constant monitoring of relative positions of the various detector elements with respect to absolutely positioned beacons is necessary. A full description of the relative positioning equipment on the string and its performance during prototype string deployments has already been discussed in section 4.5.3.

The absolute positioning of the detector is performed by acoustic triangulation of low frequency acoustic beacons placed on the string bottom and a rangemeter on a surface ship, equipped with the Dynamic Global Positioning System (DGPS). A precision of $\sim$ 1 m has already been demonstrated for the positioning of a prototype string, deployed at full immersion depth. Precise triangulation necessitates the knowledge of the sound velocity profile from the sea floor to the surface, which can be strongly distorted by thermal effects which depend on the season and current. This has to be measured by using a CTD profiler when the absolute positioning calibration is performed.

5.6.2 Timing precision and calibration

A master clock on shore, linked to Universal Time (UT) through the Global Positioning System network, permits to match events to transient astronomical phenomena such as gamma-ray bursts. The clock signal is distributed through the array network to each OM.

A LED is located in each OM, facing upwards towards the PMTs further up in the string. It can be pulsed synchronously to the clock signal. This system will enable time synchronization between adjacent storeys in the same string.

Calibration with external light sources will relay the initial calibration and monitor any possible drifts. The proposed system consists of *optical beacons* which contain high intensity pulsed light sources. They will illuminate several strings simultaneously. Ideally, the optical beacons should emit light at a wavelength as close as possible to that which is least attenuated in water ($\lambda \sim 470$ nm) and should distribute the light efficiently throughout the full solid angle with a pulse width of about 1 ns. Pulsed solid-state lasers and blue LEDs are the focus of detailed studies. Figure 5.8 illustrates the range to be obtained from such an optical beacon at various wavelengths, as a function of pulse energy.

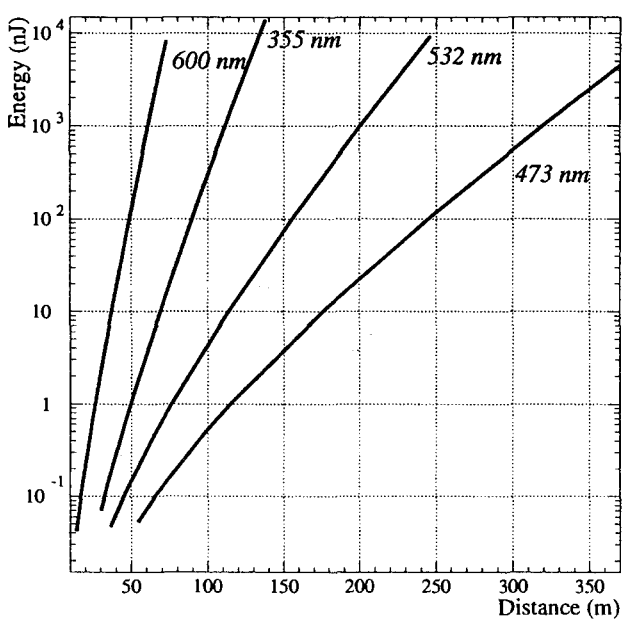

Figure 5.8: Distance in water reached by a pulse of light as a function of its energy for different wavelengths. At least 5 photoelectrons are required to be detected in the PMT.

Doubled Nd-YAG lasers which emit green light ($\lambda = 532$ nm) can be passively Q-switched to give sub-nanosecond pulses. Lasers delivering pulse energies of $\sim 1\ \mu J$ ($\sim 10^{12}$ photons) and with a time spread (FWHM) of $\sim$0.5 ns (see figure 5.9, left) have been tested. These lasers are small, easy to operate and very robust, complying with the stringent deployment and installation requirements of the experiment.

After a warming-up period of a few minutes Nd-YAG lasers show an output power stability better than 1% over several hours (see figure 5.9, right).

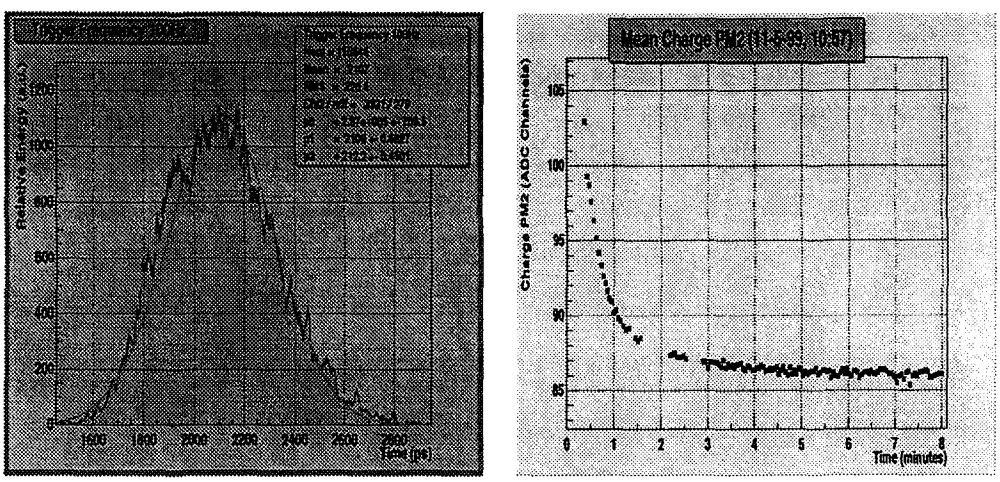

Figure 5.9: Left: Time shape distribution (picoseconds) of a Nd-YAG laser pulse as measured by a streak camera. Right: Warming-up curve (minutes) of a Nd-YAG laser as seen by a photomultiplier. After a few minutes the output power stability is better than 1% over several hours.

Simulations have been performed to estimate the reach of optical beacons using lasers together with lambertian diffusers ($\sim cos\theta$). For 1 μJ Nd-YAG lasers, distances in excess of 200 m can be reached.

A LED pulser circuit based on that of Kapustinsky *et al.* [63] has been developed using recent GaAs LEDs from Nichia and Hewlett Packard which emit in the blue ($\lambda = 470$ nm). The light pulse produced has a risetime of 2.0 ns and a duration of 4 ns FWHM as can be seen in figure 5.10 which was measured using the single photoelectron technique.

The intensity of a single flash is 50 pJ (10^8 photons). The timing jitter

between the trigger pulse and the light flash is below 100 ps which indicates that, it is possible to enslave large numbers of such flasher modules together to produce bright flashes.

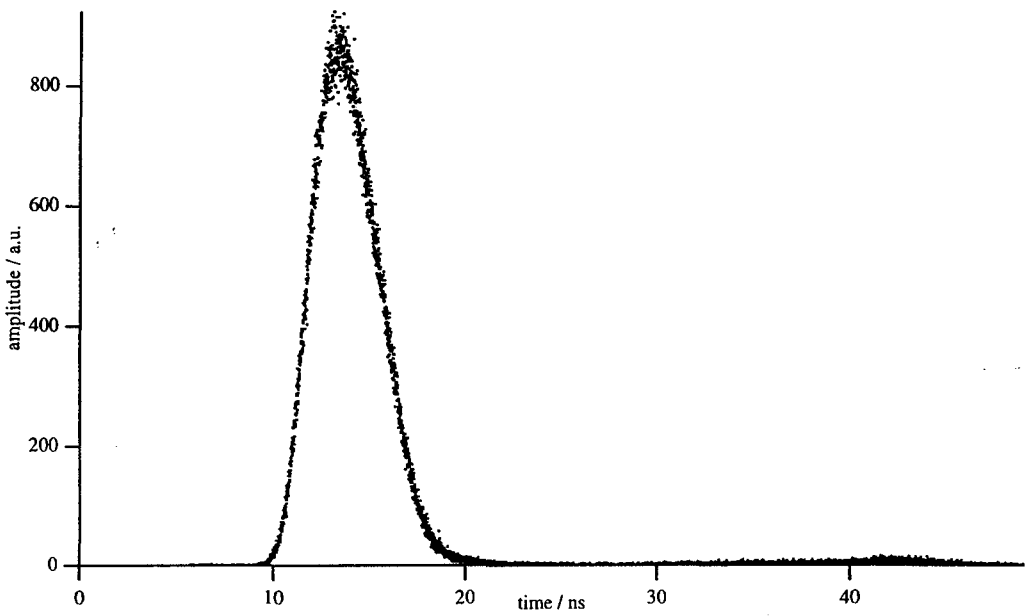

Figure 5.10: LED time response

5.6.3 Optical Module efficiency calibration

The optical module efficiency may evolve with time due to modifications of the PMT characteristics (gain, quantum efficiency, etc.), or to a change in the transmission of light from the glass sphere surface to the PMT photocathode (fouling, ageing of gel, etc.). As discussed previously, the ^{40}K present in sea water, is a natural source of single photoelectron signals. The distribution of the collected charge from such events can therefore be used to monitor the gain of the photomultipliers. An *in situ* measurement of the OM efficiency using an external calibrated light source will be a convolution of three distinct effects: the fouling of the light source itself, variations of the light transmission in sea water, and the OM's intrinsic efficiency, i.e. the change in the response of the OM in units of single photo electrons. A relative calibration can, however, be done by comparing the response of

several OMs to the high power light sources, which will be installed in the detector for the purpose of timing calibration. The light from these sources will arrive simultaneously at many OMs, allowing an accurate cross-check of the variation in amplitude response of the OMs. In the case of the Nd-YAG lasers, the accuracy of the measurement of the amplitude is limited by statistics, not by the source stability. Since the change in efficiency is expected to be a slow phenomenon, the statistical accumulation of calibration events will permit an accurate determination. In the same way, the LEDs on each storey pointing at the OMs further up the string can be used to measure the change in light transmission due to fouling and other phenomena.

To avoid problems caused by fouling of the light source, a ship-tethered calibration system is being considered for absolute efficiency calibration. This would consist of an isotropic calibrated light source enclosed in a Benthos sphere and a rangemeter to permit the accurate positioning of the source using the acoustic positioning system of the detector. An accuracy of a few tens of centimetres on distances of a few tens of metres between locations of the source in-between strings and the optical modules can be achieved and is satisfactory for our purpose. The optical module orientation with respect to the light source is determined from the tiltmeter and compass information. Sufficient fluxes of photons can be obtained by triggering simultaneously a large number of blue LEDs mounted inside a Benthos sphere. Absolute calibration of the optical modules requires that the attenuation length of light be known. This can be deduced directly from data taken with the light source at a few different positions with respect to a single optical module.

5.7 Onshore data acquisition

The object of the onshore data acquisition is to apply a level 3 filter to reduce this rate to a reasonable level for archiving on tape, maintain an experiment status database using the slow control information, and verify the integrity of the data.

The first step of the on-shore processing is event building. Here, time-stamped data from various parts of the detector are assembled into events. Most of the triggers are caused by accidental coincidences, and a customised version of the off-line reconstruction will be used to filter these.

The event building will associate both digital data from the optical modules and slow-control data in the same event. Fully built events will

be used for feedback in controlling the detector, as well as for event display and data monitoring. A Unix-based event display has been developed and tested. The programme for monitoring of slow-control parameters and event histogramming has been written and tested for the prototype string connected to shore (see section 4.5). It is based on the EPICS package and will be used in the 0.1 km^2 detector.

This page is intentionally left blank.

Chapter 6

Detector performance

The neutrino sources discussed in the scientific programme fall into two distinct categories:

- high energy neutrinos (above 1 TeV) from astrophysical sources;
- low energy neutrinos (below a few hundred GeV) for oscillation studies and from the annihilation of neutralinos.

The two classes behave differently in the detector — for example, muons from high energy neutrinos will pass right through the detector volume, whereas the low energy neutrinos may be partially contained — so both must be considered when optimising the detector design. Extensive simulation studies have been carried out on the detection of neutrinos from AGN, representing the first class of high energy astrophysical neutrinos, and on the measurement of neutrino oscillation parameters, which requires a good understanding of sub-TeV neutrinos. This chapter describes the event simulation and reconstruction, the optimisation and performance of the detector in both energy regimes, the results of the simulation studies, and a discussion of relevant systematic effects.

6.1 Monte Carlo simulation tools

This section describes the software tools used for event generation and detector simulation. Separate simulation packages are needed to treat signal events and various sources of background.

6.1.1 Event generation

Neutrinos from astronomical sources have been simulated by generating the kinematic distributions of the neutrino interactions and taking into account the absorption and energy loss of the muons in the Earth. Events are generated with a flat spectrum in both the log of the neutrino energy and in the cosine of the angle of incidence, then weights are applied according to the flux of the sources. Events are retained for analysis if there is a muon track anywhere within a distance $L = 140$ m of the instrumented detector, as shown in figure 6.1.

The main background for upward-going astronomical neutrinos comes from neutrinos produced by cosmic rays interacting in the atmosphere. For atmospheric neutrinos interacting within the volume shown in figure 6.1, tracks due to the hadronic showers, as well as those due to the muons, are generated using the LEPTO package [64]. For neutrinos interacting outside this volume, only the tracks due to the muons are simulated.

Muons originating directly from the cosmic ray showers are simulated with a single muon component and a multi-muon component. High statistics samples of single muons have been generated with a parametrization of the flux at the detector depth [65] and also by propagating the sea level flux to the detector using the package PROPMU [66]. The multi-muon component has been generated using the HEMAS package [67] with the muons propagated to the detector using PROPMU. At the present time, only relatively small samples of multi-muons have been produced.

6.1.2 Detector simulation

The response of the detector to the various types of physics events has been studied mainly using a version of the DADA program [68] which originated in the BAIKAL collaboration. This program has been modified to improve the performance at high energies and to adapt it for the ANTARES detector. In DADA, the muon is tracked using GEANT, and light coming from the secondary particles generated is parameterized for energies above 0.5 GeV for electrons, above 1 GeV for photons, and above 10 GeV for hadrons. Less energetic secondary particles are taken into account by increasing the amount of Cherenkov light emitted by the muon ($+ 18\% + 3.2\% \log E_\mu$ (GeV)). A parametrization is used for the angular and longitudinal distribution of the Cherenkov light initiated by electromagnetic and hadronic cascades [68].

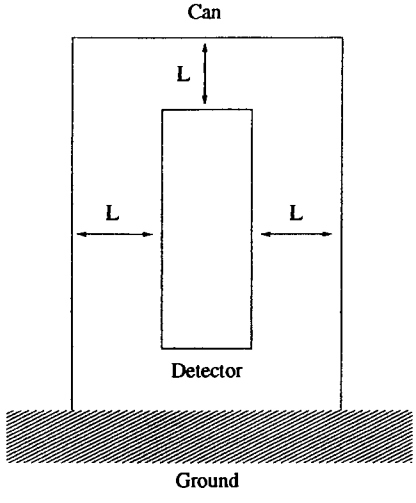

Figure 6.1: Scheme of the 'can' used for event generation. The distance L is taken as 2.5 times the maximum absorption length for light.

Checks on some of the simulation results have been made with a new program, GEASIM, developed for ANTARES. Some of the simulations of multi-muons have also been performed with the KM3 program [69] which, unlike the other programs, simulates the scattering of light in the water.

If not specified otherwise, the simulation was performed with 10-inch photomultiplier tubes. All parameters used in the simulation are based on the measurements described in section 5.3.3. The angular response simulated is that shown in figure 5.5, with a timing accuracy of 1.5 ns. For each optical module the time and amplitude of the pulse corresponding to an event is simulated taking into account the noise coming from the optical background, the gain of the photomultiplier and the effect of the electronics. All simulated events include random hits from ^{40}K in the sea water.

Photons are scattered and absorbed by sea water. DADA includes the effect of absorption, with an absorption length of 55 m unless otherwise stated, but does not include scattering. For a distance of 45 m between source and optical modules, less than 10% of the photons are scattered, so the approximation of no scattering should have little effect on the signal. Nonetheless, the scattering must be included for the background studies. No additional smearing has been incorporated into the simulations for the relative positioning of the optical modules.

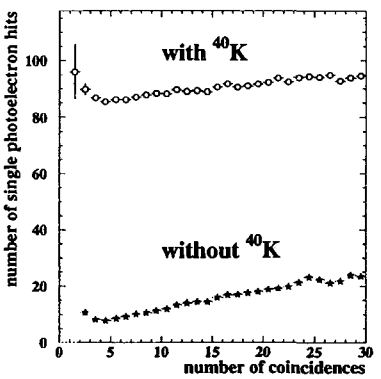

Figure 6.2: Average number of single photoelectron hits versus the number of coincidences for high energy muons, with and without optical background. The simulated background rate is 20 kHz.

6.2 Track finding and reconstruction

Before track reconstruction, a pattern recognition step is necessary to remove hits from the ^{40}K background. The hardware trigger will make requirements on the number of coincidences between two of the three optical modules in each storey of the detector. For the simulations of astrophysical performance a total of at least four coincidences on at least two different strings were required; the requirements for the oscillation study are discussed in section 6.4.1 below.

6.2.1 Pattern recognition

Figure 6.2 shows the number of hits with amplitude corresponding to one photoelectron, for a simulation of high energy muons with and without ^{40}K background. About 90% of single photoelectron hits come from ^{40}K . They cannot be removed by an amplitude cut without a large loss in signal hits.

The method adopted to remove the ^{40}K hits is to start with a track fit which uses only coincidence hits. Figure 6.3 shows the angular error of this prefit when four coincidences are required. The prefit is used to define a road in time for the selection of single hits to be used in a further fit. The hits are kept if the time difference between measurement and expectation

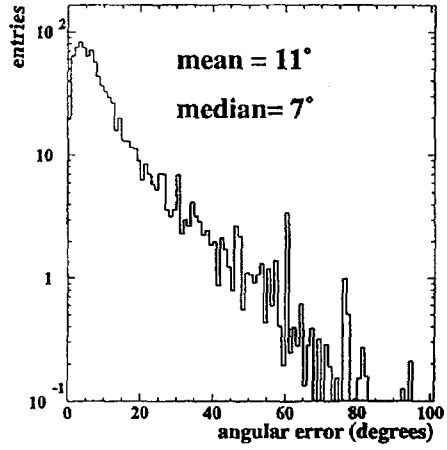

Figure 6.3: Angular error for the prefit solution for high-energy events with at least 4 coincidences on at least 2 strings, for an initial $1/E^2$ neutrino spectrum.

is between -150 and $+50$ ns and if the distance between the track and the optical module is smaller than 100 m. This selection reduces the number of hits due to the optical background by a factor of 100, while keeping 46% of the single photoelectron hits associated with the muon tracks.

6.2.2 Track reconstruction

For each optical module, the arrival time of the Cherenkov light is

$$(t_i)_0 = t_0 + (L_i + d_i \tan\theta_c)/c$$

where d_i, L_i are defined in figure 6.4, θ_c is the Cherenkov angle, and t_0 is the time at a reference point. Then $(t_i)_0$ is smeared out by the time resolution (PMT transit time spread, positioning error, scattering) to give the pulse time t_i. Photons from secondary particles will also be detected, with a distribution of arrival times that decreases exponentially with respect to $(t_i)_0$. Photons from the optical background arrive at random times.

Figure 6.5 shows the expected time distribution of the hits for different muon energies. This is the probability distribution function $P(\Delta t)$ which depends on the muon energy. In order to simplify the fitting procedure, the